Dilute Limit Alloy Pd-Cu Bimetallic Catalysts Prepared by Simultaneous Strong Electrostatic Adsorption: A Combined Infrared Spectroscopic and Density Functional Theory Investigation

Leandro De Castro[1,2], Dia Sahsah[1], Andreas Heyden[1], John Regalbuto[1], Christopher Williams[1,]*

[1]University of South Carolina, Columbia, South Carolina 29088 (USA)

[2]University of the Philippines Los Baños, Laguna, 04031 (PH)

*Corresponding author. Email: WILLIA84@cec.sc.edu

Keywords: Dilute Limit Alloy, Single Atom Alloy, CO-FTIR, DFT

Abstract

Well-defined single-atom catalytic sites with unique geometric and electronic properties are at the forefront of catalyst research. One type of SAC is a so-called dilute limit alloy, where single metal atom sites are supported on (or in) the surface of a second metal. This contribution explores the simple and scalable approach of strong electrostatic adsorption (SEA) to synthesize silica-supported dilute limit alloy (DLA) of palladium on copper. The catalysts were characterized using X-ray diffraction, temperature programmed reduction and TEM images to confirm the presence of tightly distributed metal nanoparticles. The isolated Pd sites on Cu were probed using transmission Fourier-transform infrared (FTIR) spectroscopy during adsorption of CO. Through spectral curve-fitting to extract Gaussian peak parameters, coupled with density functional theory (DFT) calculations, the nature and structure of the Pd sites was determined. In addition to typical vibrational features observed for CO on copper, three additional peaks at 2046, 2021 and 1908 cm^{-1} were observed for the dilute limit alloy Pd-Cu system. The DFT analysis of the same system showed that these peaks are consistent with CO linearly adsorbed on an embedded palladium atom on a Cu(100) surface, a Pd on a Cu(111) surface, and a bridge CO between Pd and Cu with the Pd embedded on a Cu(211) surface, respectively. Experimental and computation trends in CO vibration wavenumber could be well interpreted using the Dewar-Chatt-Duncanson (DCD) model. The promise of the SEA approach for producing DLAs and the utility of this combined FTIR/DFT approach for their characterization will be discussed in light of these findings.

1. Introduction

The promise of atom-efficient utilization of precious metals combined with the potential for unique catalytic applications drives recent efforts to develop novel synthesis methods and characterization techniques for single-sites heterogeneous catalysts (SSHC).[1,2,3–5] Such well-defined (and more uniform) active sites may also allow for a more straightforward interpretation of reaction kinetics and mechanisms through experimental evaluation and computational methods.[6,7] Isolating a known active metal (e.g., Pd, Pt, etc.) in a "sea" of another metal is a known strategy to produce a type of single-site catalyst. Such DLA might have unique properties if the electronic structure of the isolated metal is altered or the resulting isolated site geometry causes an ensemble effect. Decreased utilization of the active (often precious) metal with similar or enhanced catalytic performance would increase atom efficiency.

Several reports have appeared in the literature that show the effectiveness of DLA catalysts for a range of reactions. For example, pioneering work by Flytzani-Stephanopoulos and co-workers explored small surface concentrations of palladium atoms dispersed on a Cu(111) surface and alumina-supported Cu particles ($Pd_{0.18}Cu_{15}/Al_2O_3$). Significant improvement was observed for the selective hydrogenation of phenylacetylene to styrene relative to monometallic palladium catalyst.[8] The higher selectivity was attributed to spillover of Pd site-dissociated hydrogen atoms to the Cu surface, thus allowing the inactive copper to serve as an effective bifunctional hydrogenation catalyst. Silica-supported Pd-Cu DLA prepared in the same manner were also found to be active in selective oxidation of methanol towards methyl formate at low temperatures. In this case, the high selectivity is due to the formation of an atomically dispersed Pd oxide active site on the copper matrix.[9] Selective oxidation of methacrolein with methanol to methyl methacrylate was also enhanced by doping isolated Ni atoms on the Au surface. The single atom of nickel acted as

a binding site for methanol, as a base to stabilize the reaction intermediate and increase the number of Au-Ox active sites.[10] Improvements in dehydrogenation (NiCu), selective partial hydrogenation (PtCu), selective hydrogenation (PdAg, PdAu), and hydrogenolysis (PtCu) were also made with the use of DLA catalysts.[11–15]

These promising results using DLAs have motivated researchers in both computational and experimental catalysis.[16,17] Computational studies readily allow for exploring metal combinations to target a specific reaction and can also aid in the interpretation of experimental results.[18,19] However, while the structures of single metal alloy active sites are relatively simple (compared to standard bimetallic catalysts), the synthesis of such structures is challenging. A variety of methods have been used with varying success and complexity. Galvanic displacement (GD) has been successfully applied to make a variety of single metal alloy catalysts.[8,12,20] For example, Flytzani-Stephanopoulos et al. dispersed Pd atoms alloyed on a Cu metal nanoparticle surface on alumina support via galvanic displacement of Cu by Pd.[8] The method was extended to prepare NiCu[8] and PtCu[9,10] DLA nanoparticles supported on silica and alumina, respectively. One limitation of this method is the reduction potential compatibility of the two metals involved. Second, the metal to be displaced must be present in a reduced state, requiring inert gas protection during the GD process.

Another method has been proposed by Zhang and co-workers (2015), which involves the formation of hydroxide species $M(OH)_z$ on a reducible oxide support A_xO_y. Calcination then forms M-O-A bonds between the singly dispersed $M(OH)_z$ and A_xO_y, followed by a controlled reduction to remove some oxygen atoms to form isolated M_1A_n sites.[22,23] The reduction of precursors is crucial in preparing the catalyst, and the approach is limited to reducible oxide supports. In the vapor phase, atomic layer deposition of a second metal onto a metal nanoparticle has been

explored.[24–27] For example, Wang et al. used a combination of deposition-precipitation of Ni followed by selective atomic layer deposition of Pd to produce single metal alloy PdNi on silica. The ALD method was able to selectively target the Pd onto the Ni surface rather than on the silica support surface. However, this selective ALD procedure has only been demonstrated for silica support.[28]

Recently, Filie et al. (2021) prepared a dilute PdAu nanoparticles supported on raspberry-colloid-templetated (RCT) silica. It is a three-step synthesis method involving intitial synthesis of monometallic and narrowly-sized (~5nm) gold nanoparticles (NPs). Dilute bimetallic Pd_xAu_{1-x} was prepared by adding palladium (II) nitrate hydrate ($Pd(NO_3)_2$ to a solution containing as-synthesized Au NPs and ascorbic acid aqueous solution. Lastly, these bimetallic nanoparticles were then delivered to silica support using the RCT approach. [29]

More traditional co- and sequential- incipient wetness (IW) impregnation methods have also been used to make single metal alloy catalysts.[30–35] For example, Pd-Ag/SiO_2 with dilute levels of Pd were synthesized using nitrates as precursors.[36] The resulting improvement in activity and selectivity for hydrogenation of acrolein was attributed to the addition of atomically dispersed Pd. However, as is typical with IW methods, the particle sizes were on the order of 5-9 nm, which is not a high degree of dispersion.

One key consideration in designing a single atom alloy catalyst is the possible segregation of the active isolated surface atom into the bulk phase of the abundant host metal. Zhang et al. (2015) reported surface atom migration during the galvanic replacement of Pd on Ag metal surface due to the large difference in surface free energy. Pd tends to diffuse to the bulk of the base Ag particle and vice-versa, providing fresh Ag atoms for galvanic displacement.[13] Thermodynamic limitations depending on the surface free energies dictate how a given metal would preferentially segregate

105 to a nanoparticle surface, thus possibly avoiding bulk migration. In addition, for a given reaction,
106 the strong interaction of a single metal site with a specific adsorbate (e.g., CO) might serve to
107 stabilize the atom on the surface. In the context of ultrasmall bimetallic catalysts as prepared by
108 Wong et.al. (2017), the significantly low number of bulk atoms provides a low probability for an
109 isolated surface atom to bulk segregate. In a cuboctahedron cluster model developed by Benfield
110 (1992), a copper particle having a 1.49 nm particle diameter (m=4, a=0.362 nm) has ~63% of its
111 atoms on the surface.[37] This high probability of surface atoms as the particle size decreases is the
112 motivation for the synthesis of isolated surface atoms using the co-SEA method. This strategy
113 would allow for facile one-pot synthesis of any dilute limit alloy bimetallic catalyst (DLA) using
114 the method of simultaneous strong electrostatic adsorption (co-SEA).[38]

115 One challenging aspect of isolated metal atoms is characterization due to their inherent small
116 concentration in the catalysts. X-ray photoelectron spectroscopy (XPS) typically does not provide
117 a high enough signal for the isolated atoms and would require a synchrotron beam line for a
118 brighter X-ray source.[39] Aberration corrected scanning transmission electron microscopy (AC-
119 STEM) can be used to distinguish between a single atom and neighboring atoms when there is a
120 high atomic number difference (i.e., Z-contrast) but is often challenging when the atoms are similar
121 in size.[40] Other techniques such as temperature programmed reduction (TPR), may provide
122 information about the interaction between the dilute metal and its host, but not the direct surface
123 environment.[41,42]

124 One approach that shows some promise for characterizing single atom alloy catalysts is Fourier
125 transform infrared spectroscopy (FTIR) of CO adsorption. The highly sensitive signal can allow
126 the vibrational properties of various single atom sites to be explored. FTIR is a well-established
127 method used to characterize monometallic and bimetallic catalyst surfaces. A significant number

of publications have been published for most of the metals used in catalysis. Sheppard and Nguyen (1978) consolidated IR results from various studies (single crystals and oxide supported metals) and suggested schemes for interpreting spectral results. In the recent review made by Sheppard and De la Cruz on the reliability of vibrational spectroscopy for structure identification of chemisorbed species such as CO on (111) surfaces, they concluded a 2130-2000 cm^{-1} range for linear (on-top) sites and an extended range 1950-1800 cm^{-1} for 3-fold (hollow) bridge CO overlapping with 2-fold bridge CO in the range 2000-1870 cm^{-1} at higher coverage.[43] FTIR characterization of CO adsorption is relatively straightforward for monometallic catalysts since the CO surface species are associated with only one metal (albeit with various coordination and geometric structures). For a bimetallic catalyst with only one metal adsorbing CO, spectra analysis can be similar to that of the monometallic counterpart[13]. However, in systems where both metals adsorb CO, the resulting spectra involve a convolution of vibrational features that can make even a qualitative analysis challenging.[44,45]

In this study, silica-supported Pd-Cu bimetallic catalysts were synthesized using a dilute limit approach involving simultaneous strong electrostatic adsorption (co-SEA).[41,42] The molar ratio of Pd to Cu was varied in an attempt to achieve single atom alloy sites of Pd on Cu. These catalysts have been characterized by a range of structural approaches, and especially with FTIR during CO adsorption, to probe the evolution of the Pd_1Cu single metal alloy sites. Extensive spectral curve fitting over a range of conditions was used to identify unique vibrational features, which were then confirmed using density functional theory (DFT) modeling of various adsorbed species. This powerful combination of experimental and computational approaches revealed the presence of two types of single atom Pd_1Cu species that appear in the dilute limit.

2. Experimental and Computational Details

151 **2.1 Experiments.**

152 **Catalyst Preparation.** Evonik Aerosil 300® (BET=304 m^2/gm) was used as silica support for
153 adsorption with a surface loading of 1000 m^2/L. Metal precursors used are copper (II) nitrate
154 hydrate (Sigma-Aldrich 99.999%) and tetraamminepalladium (II) chloride monohydrate (Sigma-
155 Aldrich 99.99%). Dilute limit alloys of palladium-copper supported on silica were prepared by
156 simultaneous strong electrostatic adsorption (co-SEA), which has been described previously.[41]
157 Silica supported monometallic palladium, and copper catalysts were also prepared using the same
158 method but using only the associated single metal precursors. Silica was poured into an ammonium
159 hydroxide-adjusted solution (pH 12) containing cationic palladium and copper ammine complex
160 precursors. In making the dilute limit alloy, a palladium to copper metal ratio range from 1:15 to
161 1:60 with an initial metal concentration based on one monolayer theoretical surface adsorption
162 density (~1.2 μmole/m^2) for metal ammine complexes were prepared.[42,46] Silica having a PZC=3.6
163 deprotonates at pH > PZC and develops the negatively charged surface, thereby allowing for the
164 strong adsorption of one monolayer of hydrated cationic ammine complex on the surface. The
165 mixture was placed in an orbital shaker for 15 minutes, and the support was recovered using
166 vacuum filtration. The recovered silica containing the adsorbed precursors was dried at room
167 temperature for at least 12 hours, followed by a muffle furnace oven drying at 120 °C for 4 hours.
168 Finally, the catalysts were reduced in a horizontal tubular furnace under a gas mixture of 20% H_2
169 balanced N_2 with a total flow rate of 500 SCCM. A ramp of 5 °C/min to 400 °C and a soak time
170 of 1 hour were employed.

171 **Catalyst Characterization:** Aliquots of solution were taken before and after contact with the
172 support to determine metal adsorption. Metal concentrations were measured using a PerkinElmer
173 Avio 200 inductively-coupled plasma optical emission spectrometer (ICP-OES) using

multiwavelength calibration, multiple replicate data, and multiple view mode. The samples were diluted to minimize the effect of highly volatile compounds on plasma stability.

X-ray diffraction (XRD) patterns were obtained using a Rigaku MiniFlex II equipped with a high sensitivity D/tex Ultra Si slit detector. Patterns were recorded from 10-80° 2θ using a step size of 0.02°, and a Cu-Kα radiation source (λ=1.5406 Å) operated at 30 mA and 15 kV.

X-ray photoelectron spectroscopy (XPS) investigation of untreated and treated catalysts was carried out using a Kratos AXIS Ultra DLD XPS (Kratos Analytical). The XPS system is equipped with a monochromatic Al Kα source operated at 15 keV and 150 W, a hemispherical analyzer, charge neutralizer, catalyst treatment cell, and a load lock chamber for rapid introduction of samples without breaking vacuum. The X-rays were incident at an angle of 45°, with respect to the surface normal. Analysis was performed at a pressure of ~1×10^{-9} mbar and high-resolution core level spectra were measured with a pass energy of 40 eV. The XPS experiments were performed by using an electron beam, directed on the sample, for charge neutralization. The curve fitting procedure was carried out using the XPS Peak 41 software and the peak approximation was carried out by a combination of Gaussian - Lorentzian functions, with subtraction of Shirley-type background. The in-situ reduction of the catalysts was performed in a reaction cell (Model: ES-009R01) directly attached to the XPS chamber, which allows the sample to be treated at gas flow conditions. The samples were transferred inside the reaction cell and back to the analysis chamber without exposure to the atmosphere.

Scanning transmission electron microscopy (STEM) images were obtained with a JEOL 2100F 200kV FEG-STEM/TEM equipped with a CEOS Cs corrector on the illumination system. The equipment was controlled to have an aperture of 17.5 mrad, which at 200 kV provides a nominal probe size of<0.1 nm. High angle annular dark-field (HAADF) STEM images were acquired on a

Fischione Model 3000 HAADF detector with a camera length such that the detector spanned 50–191 mrad. The dwell time per pixel was 15.8 μs. The samples were prepared for STEM by dropping the powder onto 300 mesh Cu grids coated with a holey amorphous carbon film.

TPR was performed on the oven-dried catalysts by using a Micromeritics 2920 equipped with a TCD. The temperature was set at a ramp rate of 5°C/min, and the reducing gas of 10% H_2 balanced Ar was set at a flow rate of 50 SCCM.

A Nicolet Nexus 470 spectrometer equipped with liquid nitrogen-cooled MCT-B detector was used in transmission to obtain a series of transient CO adsorption spectra with a resolution of 2 cm^{-1} averaging 32 scans using a single beam mode. Catalyst samples were compressed to obtain self-supporting 12 mm thin disks with a density for a given thickness of approximately 25 mg/cm^2. The sample is contained inside a transmission cell made of 10 cm long stainless steel capped with IR-transparent NaCl windows on both ends that are cooled with flowing coolant. The cell body is wrapped with heating tape and is heated using a temperature controller. A thermocouple is located near the sample to monitor temperature during sample pretreatment and measurement. In situ drying and reduction pretreatment were performed prior to each measurement. Samples were dried for 1 hour at 100°C with flowing nitrogen gas. Upon cooling to room temperature, the samples were then reduced at 400°C for 1 hour in a 20% H_2 balanced N_2 gas mixture with a total flow rate of 250 SCCM. A ramp rate of 5°C/minute was used in both the drying and reduction steps and only the cooling steps use nitrogen gas. A series of spectral measurements, with background spectra measured with nitrogen gas flowing, were recorded in 3 minutes intervals starting with the introduction of 1% CO/He. The first stage (CO adsorption) involves measurements starting with the introduction of CO gas into the system until saturation condition within 90-120 minutes. The second stage (N_2 purging) starts upon replacing the CO gas mixture with nitrogen gas until a final

purge spectrum at approximately 90-120 minutes. All measurements were made under atmospheric pressure and room temperature.

Spectral fitting using Gaussian functions was made according to scheme 1. Prior to fitting the dilute limit alloy spectra, the corresponding monometallic spectra were deconvoluted and fitted first. A review of the adsorbed CO vibration wavenumber found in the literature was made for each metal to determine the spectral similarities and peaks observed. Curve fitting for the series of spectra was made using a general purpose curve fitting program Fityk[47]. The optimized Gaussian function widths (FWHM) of the relevant peaks are kept the same across a given series of spectra. The peak center wavenumber and height/area were allowed to change from spectrum to spectrum. Thus, for the purpose of analysis, it was assumed that the FWHM values of the contributing adsorbed CO peaks do not change as a function of their intensity. In the case of spectra from the Pd-Cu system, the obtained Gaussian functions from the monometallic copper fitting were used as part of the starting set of fitting functions for the bimetallic catalyst spectra. The same FWHM and peak ratios from monometallic copper were used to obtain the contributions from adsorbed CO on copper. Additional Gaussian functions associated with isolated palladium were then included in the fitting using the series of spectra obtained during the N_2 purging stage. The set of Gaussian functions for monometallic palladium were also included in the fitting function to determine any presence of isolated monometallic palladium nanoparticles. All deconvoluted spectra presented on this paper converge with an R-square above 0.99 and a residual standard deviation of less than 0.002.

Scheme 1 General fitting scheme for dilute limit alloy bimetallic catalyst.

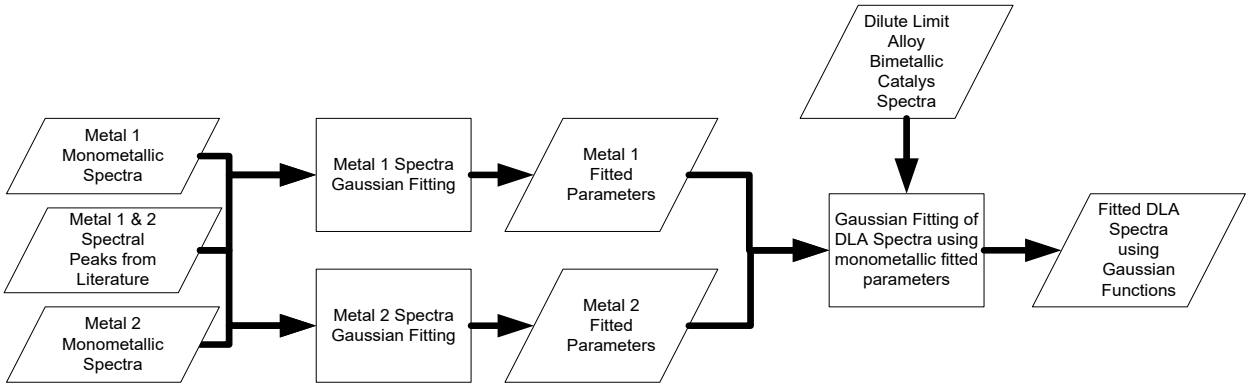

241

242

243 2.2 Computational Methods

244 First principle calculations were performed using non-spin polarized plane-wave Density
245 Functional Theory (DFT) as implemented in the Vienna Ab-initio Simulation Package (VASP
246 5.4.4).[48,49] A frozen-core, all-electron projector augmented wave (PAW)[49,50] approach was used to
247 describe the electron-ion interactions. The Revised Perdew-Burke-Ernzerhof (RPBE) functional
248 proposed by Hammer *et al*.[51] was used to treat the exchange-correlation effects. Compared to other
249 functionals within the Generalized Gradient Approximation (GGA), RPBE functional is reported
250 in the literature to predict accurate adsorption geometries for adsorbed CO over transition
251 metals.[52–54] In particular, RPBE predicted experimentally observed CO adsorption sites over
252 several facets of Cu.[55]

253 Basis sets included wavefunctions with kinetic energy up to 600 eV. A 1.0×10^{-7} eV
254 convergence criterion was set for the electronic Self-Consistent Field (SCF) loops. Structures were
255 considered relaxed when the maximum force on any atom was less than 0.01 eV/Å. Harris
256 corrections based on the Harris-Foulkes formalism[56,57] have been applied to the forces and stress
257 tensors, and the total energy was corrected for dipole effects using a modified version of the
258 Makov-Payne scheme.[58] The Brillouin zone was sampled using a Monkhorst-Pack[59] $4 \times 4 \times 1$ k-
259 point grid. First-order Methfessel-Paxton[60] smearing ($\sigma = 0.10$ eV) was used to speed up the

convergence of reciprocal space integrals with respect to the number of k-points. Bulk lattice constants for FCC-Cu and FCC-Pd were calculated to be (a_{Cu} = 3.672 Å) and (a_{Pd} = 3.972 Å), values that are in good agreement with reported experimental values of (a_{Cu} = 3.597 Å) and (a_{Pd} = 3.859 Å).[61] Different CO-metal surface complexes were modeled using slab models consisting of 4 surface layers. For the (111) and (100) surface models we used supercell of size (3 × 4) . A (2 × 3) supercell was used for the (211) and (110) surface models. For the embedded site models, a single Cu surface atom was replaced with a single Pd atom. For ad-atom site models a single Pd atom was located over the surface in the energetically most favorable position. For all surface models, the Pd surface concentration is 1/12 ML (1/13 ML for the ad-atom models), except for (211) where we have a surface concentration of 1/18 ML. The top two layers were relaxed in all calculations while the bottom two layers were fixed to their bulk positions. A vacuum space of 15 Å was added along the perpendicular to the surface normal to ensure that the charge density trails off to zero along the surface normal. Such a vacuum gap is also sufficient to ensure that slabs do not interact with their periodic images in the vertical direction.

Harmonic vibrational frequencies were calculated using a numerical computation of the Hessian matrix using the tools implemented in the VTST package for VASP developed by the Henkelman group.[62] Numerical calculations needed to compute second derivatives of the energy were performed using the central-difference approximation, wherein the adsorbate atoms were displaced by 0.005 Å from their equilibrium positions. To account for the systematic deviation between DFT-calculated vibrational frequencies and experimental frequencies[63,64], a scaling factor of 1.0314 was applied to the RPBE frequencies. The scaling factor was selected such that the scaled calculated C—O stretching frequency in the gas phase is equal to the experimental value of 2170 cm^{-1}.[65]

3. Results and Discussion

3.1 Characterization of Catalysts

Calculated nominal weight loadings and surface densities of as-synthesized monometallic palladium and copper catalysts and dilute limit alloy Pd-Cu bimetallic catalysts are shown in Table 1. The weight loading of monometallic palladium is comparable with that of the bimetallic catalysts. Applying the synthesis method of Wong et al. (2017), the adsorption of the copper complex on an amorphous silica surface falls within the theoretical monolayer predicted for strong electrostatic adsorption of ammine complex precursor (~1.2 μmole/m^2).[46] This suggests the absence of copper dimer formation as observed in previous works wherein the amount of adsorbed copper is beyond one monolayer of theoretical adsorbed precursor retaining one layer of hydration sheath.[42,66] The observed total surface density also conforms with the maximum density observed in the uptake survey for the Pd-Cu co-SEA system.[41]

Table 1. As synthesized silica-supported Pd, Cu and dilute limit Pd-Cu catalyst weight loading

Catalyst	Measured Molar Cu/Pd Ratio	Weight Loading, wt%		Surface Density, μmole/m^2		
		Pd	Cu	Pd	Cu	Total
Pd		0.09		0.028		0.028
Cu			2.38		1.217	1.217
1Pd-15Cu	19/1	0.19	2.21	0.06	1.13	1.187
1Pd-30Cu	36/1	0.11	2.35	0.034	1.205	1.238
1Pd-60Cu	74/1	0.05	2.34	0.016	1.197	1.213

Within the limit of high-resolution XRD, the powder diffraction pattern (Figure 1) for both the SEA-prepared monometallic and bimetallic catalysts show the absence of sharp peaks for the

palladium and copper grain. In comparison, a similar loading monometallic copper prepared by dry-impregnation shows the presence of a larger copper grain size (Figure 1). The pattern suggests a small particle size (<2 nm) typical for catalysts prepared by SEA due to the strong metal precursor-support interaction that limits atom migration during nanoparticle formation.[41,67] The particle size also conforms with the STEM image obtained for the bimetallic Pd-Cu system (Figure S1).

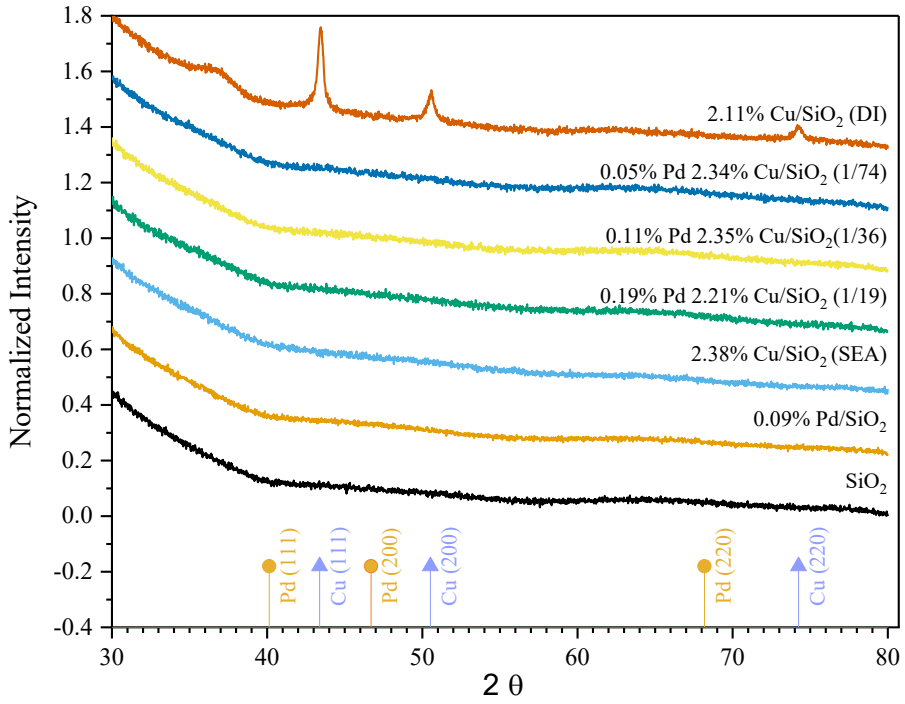

Figure 1. Powder X-Ray Diffraction Pattern for Cu, Pd and Dilute Limit Alloy Pd-Cu Catalysts.

The H_2-TPR profiles provide insight into how the strongly adsorbed precursors become reduced to form metal particles. In Figure 2, the peak reduction temperature of a series of increasing dilution of palladium in copper shows that the reduction peak position shifts towards that of monometallic copper. Nevertheless, at a dilute amount of palladium, the reduction peak of the copper metal precursor is decreased significantly (~15 °C), confirming a close interaction between

the two metals. Since the palladium precursor reduces first (peak at 156 °C), these reduced Pd atoms dissociate H_2 to H atoms[68], which spillover and reduce the copper at a lower temperature.

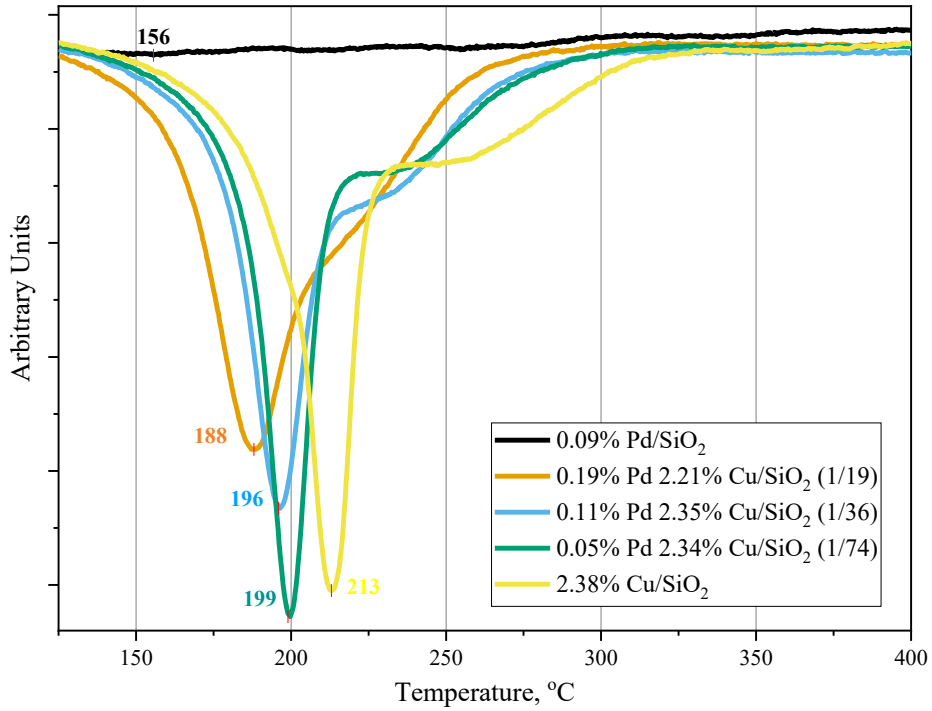

Figure 2. H_2-TPR of Pd, Cu and dilute limit alloy Pd-Cu dried catalyst prepared by strong electrostatic adsorption.

XPS measurements show identical behavior in Cu 2p binding energy for both the monometallic copper and bimetallic dilute limit alloy catalyst. Two peaks were observed for $Cu(OH)_2$ (B.E. = 936.4 eV)and CuO (B.E. = 934.1 eV) species for pre-reduced samples exposed to atmospheric conditions. After in-situ reduction, only one peak corresponding to a fully reduced copper (Cu^0) (BE=932.5 eV) was observed. XPS measurement of this reduced copper after CO exposure shows two peaks with higher binding energy (Figure S2a & S2c). The 933.1 eV peak is associated with bridge CO while the 934.6 eV peak is attributed to linear CO. The adsorbed CO on the copper surface has its anti-bonding π bond orbitals filled by electron π-backdonation, thereby losing

electrons from the copper metal surface. In an ambient pressure XPS study by Zhang and Ptasinska (2016) on Cu crystals, the shift in Cu 2p was not observed but instead the existence of shake-up peaks suggests CO interaction with Cu.[69] The same increase is observed for the Pd 3d binding energy after CO exposure in the present study (Figure S2b & S2d). An increase in B.E. of Pd 3d from 335.2 eV for the reduced isolated Pd on copper to B.E. 335.9 eV with the Pd-CO system. In a NAP (near ambient pressure)-XPS study by Bukhtiyarov et al. (2018) on Pd-Au bimetallic catalysts, they found the same blue shift in B.E. from Pd state (B.E. =334.7 eV) to Pd-CO state with linear and bridge CO contribution (B.E=335.6 eV and B.E.= 336.2 eV, respectively).[70,71] The Pd-Cu DLA also shows the same trend as that of monometallic Cu, which suggests the absence of electron transfer between Pd and Cu atoms. This could be attributed to strong metal-support interaction that overshadows the electron transfer between Pd and Cu atoms. Spectra for C 1s suggest an adsorbed CO giving a binding energy at ~289.8 eV (Figure S3). The increase in oxygen atomic % in all samples upon CO exposure comes from the CO adsorbed on the metal surface (Table S1-S3). The increased C-C peak after CO exposure for both monometallic copper and Pd-Cu DLA suggests a decomposition of adsorbed CO on the surface (Figure S3a &S3c, Table S4). In a study by Ichikawa, S. et al. (1985), they found disproportionation of CO to CO_2 and carbon on a small palladium particles on a silica support.[72] They found a decrease in CO chemisorption sites after seven cycles of CO adsorption and desorption at elevated temperature. At mild temperature, CO disproportionation was observed by Li et al. (1991) on partially reduced cerium oxide using FTIR spectroscopy.[73] Although the XPS experiment of CO exposure were made in high vacuum system, the disproportionaion of CO during the CO exposure stage is not known. The potential effect of this is the loss of site for CO adsorption that could lower signal (e.g. CO-FTIR) for the Pd-CO isolated sites due to surface poisoning.

3.2 FTIR of Adsorbed CO

To probe the surface of the dilute limit alloy catalysts prepared by co-SEA, FTIR spectra were obtained during and after exposure to CO. In addition, spectra of monometallic Cu and Pd catalysts (at similar loadings found in the dilute limit alloy samples) were also acquired for comparison. The in-situ reduction performed prior to CO-FTIR was confirmed by XPS to result in reduced metal surface (see Supporting Information, Figure S2). Selected background-corrected spectra are reported to show the relevant trends, with the full sets of raw spectra provided in the supporting information (Figure S4). With the given dilute metal ratio, the amount of isolated atom present in one cluster would depend on the total number of atoms comprising one particle. In this study, the dynamic behavior of the spectra of the monometallic catalysts (Cu) was observed from the start of CO introduction to the final N_2-purged spectra.

It should be noted that several studies have shown that exposure to CO can result in surface segregation of Pd in bimetallic PdAu[71] and PdAg[74] systems. While this possibility cannot be ruled out in the present case, such behavior would not alter the present conclusions, since analysis of CO adsorption was performed on steady state spectra after saturation and N_2 piurging. To clearly determine this would require the use of near ambient-pressure XPS and x-ray absorption spectroscopy measurements that are beyond the scope of the present study.

3.2.1 Monometallic Copper and Palladium Catalysts

Selected spectra obtained during transient CO adsorption and N_2 purging are shown in Figure 3 for monometallic copper. At the onset of CO adsorption, the band intensity in the region 2070-2140 cm^{-1} immediately reached its highest intensity. However, upon continuous exposure to CO, the band envelope from 1900-2050 cm^{-1} gradually gains in intensity while the 2070-2140 cm^{-1}

region decreased slightly. This transition also produced an isosbestic point at 2070 cm^{-1}. The entire band envelope became stable after 90 minutes of exposure, with two peaks becoming prominent at 2050 cm^{-1} and 2010 cm^{-1} near the end. When the CO gas was purged with N_2, both the 2070-2140 cm^{-1} region and the 2050 cm^{-1} peak intensities rapidly decreased while the 2010 cm^{-1} peak increased beyond its CO-saturated intensity. Another isosbestic point at 2030 cm^{-1} was also visible during this transition but not as clear due to the transient nature of the experiment. It is also evident that the 1900-2000 cm^{-1} region slightly increased in intensity.

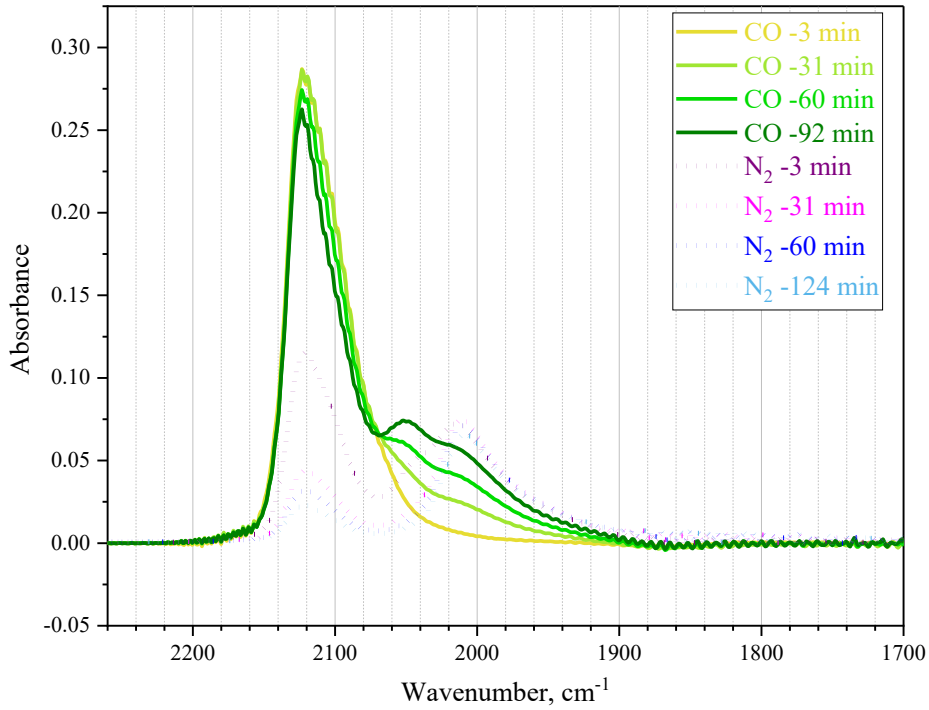

Figure 3. Selected blank-subtracted transient spectra for CO adsorption and desorption on monometallic copper catalyst.

Figure 4 shows the fitted functions from the saturated CO spectra to the final N_2-purged spectra. From these fits, the integrated areas of each associated peak were obtained and are plotted versus time in Figure S5a. The total integrated intensity during the CO exposure stage shows a gradual

increasing trend suggesting the transformation of adsorbed species upon prolonged CO exposure. Figure S5 reveals that the 2104 cm^{-1} peak decreased while the peaks in the region 1970 cm^{-1} to 2050 cm^{-1}increased, indicating a probable switch in adsorption mode. In the FTIR study by Hadjiivanov et al. on Cu/SiO_2, adsorbed CO species were observed at 2045 and 2018 cm^{-1}, with the former dominating at high CO partial pressure and the latter at low CO partial pressure. The 2045 cm^{-1} peak was assigned to the asymmetric stretch of the *gem*-dicarbonyl. The *gem*-dicarbonyl species transitioned to monocarbonyl at 2018 cm^{-1}.[75] The second expected peak associated with a dicarbonyl CO species was not evident in their spectra due to the possible masking of a Cu^0-CO band at 2129 cm^{-1}. In the present case, during the N_2 purge, the 2104 and 2050 cm^{-1} peaks decreased markedly, and their ratio remained approximately constant. From this trend, we assign the 2104 cm^{-1} absorption as the second peak of the *gem*-dicarbonyl species together with the 2050 cm^{-1} peak analogous to the dicarbonyl as proposed by Hajiivanov et al. Also, the increase in integrated area for the 2009 cm^{-1} peak during the nitrogen purging stage could be associated with the linear CO formed from this dicarbonyl CO species. This assignment would give a ~50-55 cm^{-1} difference in symmetric and asymmetric CO vibrations which is comparable to that reported in the literature. [76,77]

The in-situ reduction at 400 °C assures that most of the copper are in a reduced state (confirmed by XPS, cf. Fig S6) given that the reduction temperature peak obtained for pure copper catalyst is at 210°C. Thus, the 2124 cm^{-1} peak is assigned to linear CO adsorbed on a reduced copper atom (Cu^0 – CO) situated in a low index terrace site. It is noted that in the literature this peak has been assigned inconsistently to Cu^0-, $Cu^{\delta+}$- or Cu^+-CO vibrations.[76,78–81] In the study by Scarano et al. (1998) on silica-supported Cu_2O, they found a 2158 cm^{-1} peak at high CO coverage and proposed it to be associated with the symmetric mode of a dicarbonyl species on monocoordinated Cu(I) on

the (111) face of Cu_2O.[76] It should be noted that the particle size under consideration is 10- to 50-times higher than the particle size in this study and the adsorption temperature is at ~100 K. Thus, the low intensity 2156 cm^{-1} peak can be attributed to unreduced copper in defect sites or corner sites[76,82]. Bridge CO was assigned to the two low broad bands at 1981 cm^{-1} and 1879 cm^{-1}, specifically associated with terrace and edge/step sites of Cu, respectively. Band assignments for monometallic copper are summarized in Table 2.

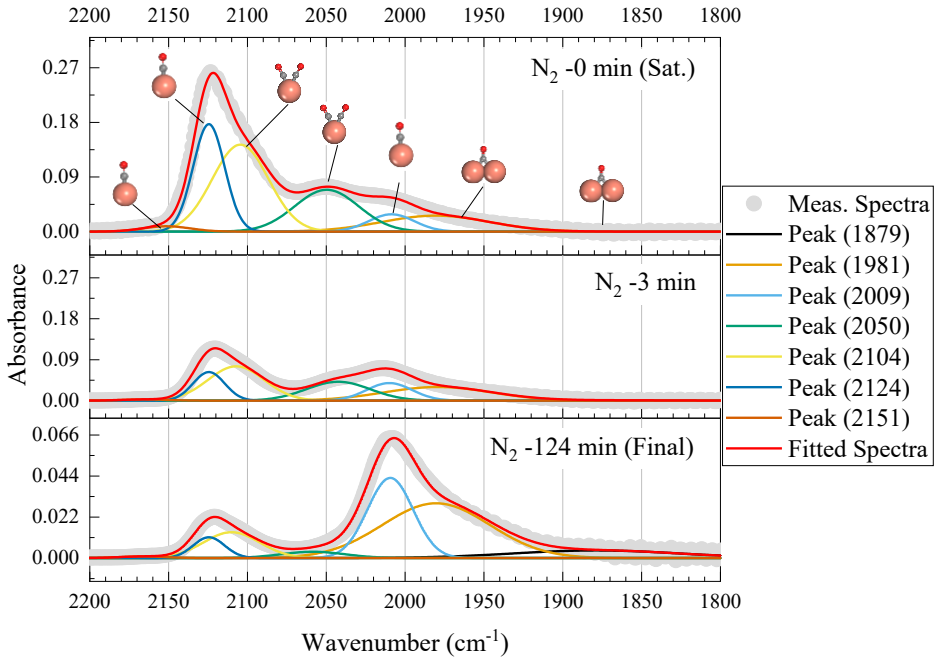

Figure 4. Fitted gaussian functions for 2.38%Cu/SiO_2 selected spectra during nitrogen purging and the corresponding Cu-CO site peak assignment.

Table 2. FTIR CO frequency surface sites assignment for monometallic copper.

Metal-CO Species	Surface Sites								
	Corners/Defects			Terraces			Steps/Edges		
	Low Cov.	High Cov.	Ref.	Low Cov.	High Cov.	Ref.	Low Cov.	High Cov.	Ref.
$Cu-(CO)_2$							(2058, 2110)	(2050, 2104)	2045[75]

Cu-CO	2167	2151	2157[83], 2154[76]	2124	2124	2129[75]	2009	2009	2003[75]
Cu_2-CO				1980	1981		1879	1879	

418

419

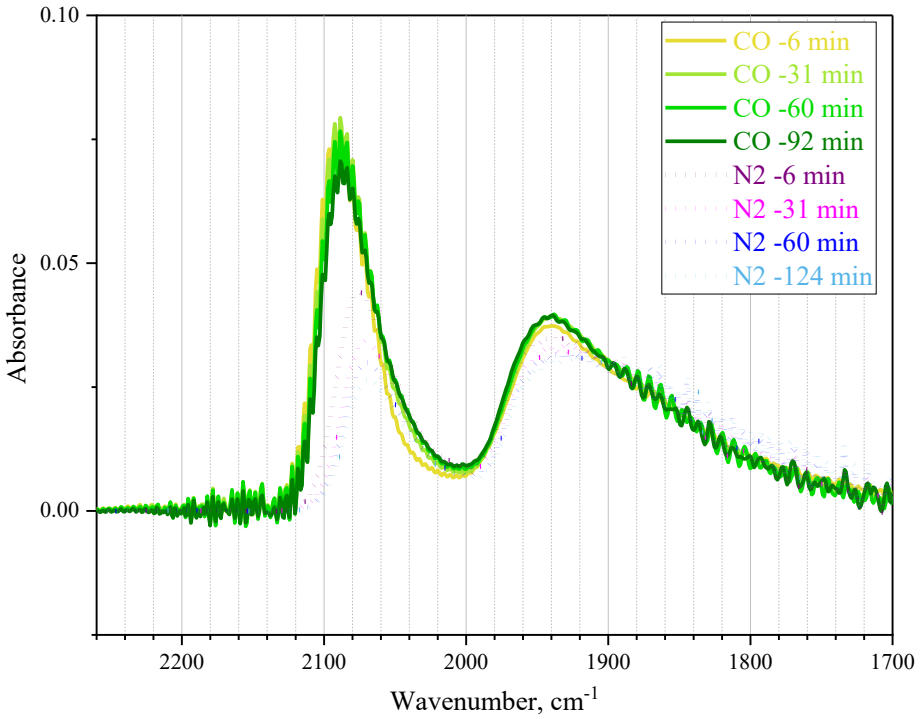

420

421 Figure 5. Selected blank-subtracted transient spectra for CO adsorption and desorption on
422 monometallic palladium catalyst.

423 Spectra obtained for 0.09%Pd/SiO_2 during CO adsorption and N_2 purging are shown in Figure
424 5. Band separation between linearly (>2000cm^{-1}) and non-linearly (<2000 cm^{-1}) adsorbed CO is
425 evident and agrees well with the literature[84–87]. The asymmetric band envelope in the linear region
426 involves a main peak at ~2086 cm^{-1} with a shoulder at ~2047 cm^{-1} becoming somewhat more
427 prominent upon longer CO exposure. Upon purging with N_2, the absorbance in this region
428 decreased but eventually reached a steady state. The non-linear region is characterized by a broad
429 and unresolved band from 1700-2000 cm^{-1}, suggesting convolution of several peaks arising from

various highly coordinated CO surface species. At saturation, this band has a high intensity peak at 1940 cm^{-1}, which decreases in intensity upon N_2 purging. Also, the shoulder at ~1800 cm^{-1} in the final purge spectra shows a relatively higher intensity with respect to that obtained at saturation.

The fitted functions from the saturated CO spectra to the final N_2-purged spectrum for Pd/SiO_2 are shown in Figure 6. Six Gaussian functions with unique constant FWHM were obtained to fit across the series of spectra. In the fitting process, two Gaussian functions were utilized for the linear region and the respective wavenumbers were allowed to shift. From initial CO introduction to saturation, the high wavenumber linear CO peak (2086 cm^{-1}) reached the saturation intensity instantly (Figure S4b) and during the desorption stage, the peak downshifted to 2069 cm^{-1}. After almost two hours of continuous nitrogen gas purging, a non-changing and lower absorption intensity was obtained in both the linear and nonlinear CO vibration regions. This observation suggests that palladium clusters were formed with the synthesis method at low weight loading and conforms with the results obtained in previous studies.[45,88]

Bardshaw and Hoffman (1978) made a thorough infrared studies on CO adsorption on palladium single crystal and proposed an adsorption band of a CO singleton. They associated the 2050 to 2120 cm^{-1} to linearly bonded CO, 1880 to 2000 to bridge CO and 1800 to 1880 to three-fold co-ordination sites. Although these assignments neglected other effects such as CO coupling, the same can be used to assign the adsorbed CO species for the fitted Gaussian functions (Table 3) in this study. In assigning linear CO to either from a terrace or edge site, the degree of electron π-backdonation to the anti-bonding orbital was used with edges sites having more available electrons hence would give a relatively lower CO stretching band wavenumber.[89]

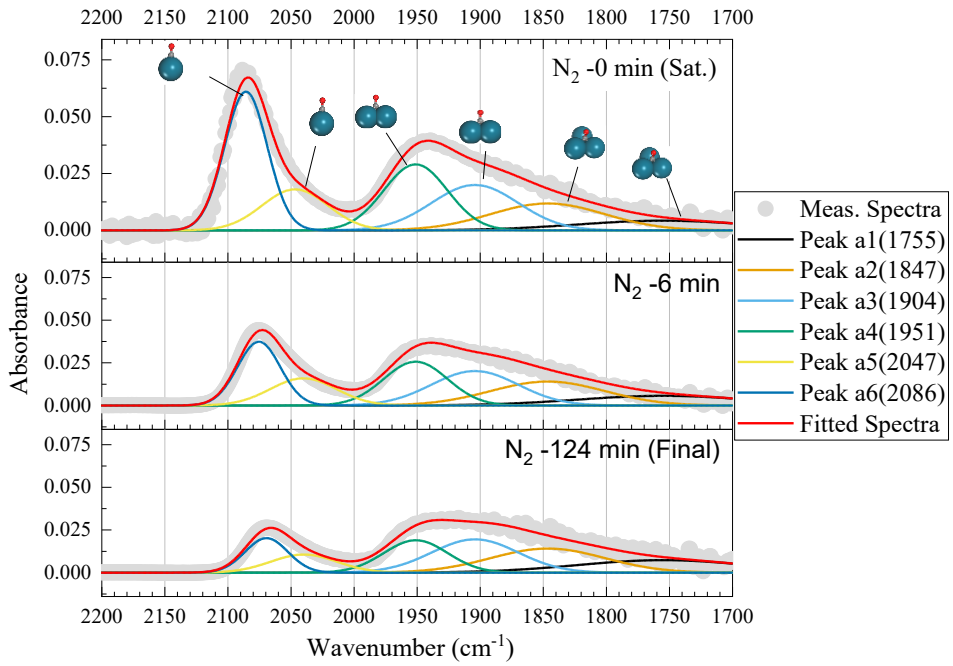

Figure 6. Fitted Gaussian functions for 0.09%Pd/SiO_2 spectra taken after 124 minutes of nitrogen purging with the corresponding Pd-CO site peak assignment.

Table 3. FTIR CO frequency and surface site assignments for monometallic palladium.

Metal-CO Species	Surface Sites					
	Terraces			Steps/Edges		
	Low Cov.	High Cov.	Ref.	Low Cov.	High Cov.	Ref.
Pd-CO	2069	2086	2095[88], 2092[90], 2077[91], 2073[92]	2038	2047	2050[91], 2049[13], 2033[9]
Pd_2-CO	1949	1951	1949[90], 1951[92], 1937[9], 1956[88]	1904	1904	1914[92]

Pd_3-CO	1847	1847	1836[90], 1840[91], 1830[88]
	1755	1755	

456

457 3.2.2 Pd-Cu Dilute Limit Alloy

458 Transient spectra for the 1/19 (Figure S6a), 1/30 (Figure S6b) and 1/74 (Figure S6c) dilute limit
459 alloy catalysts were acquired during CO adsorption and N_2 purging with the selected blank-
460 subtracted spectra shown in Figure 7a-c. Overall, the progression of the spectra is similar to that
461 obtained for monometallic copper. Two prominent features at ~2050 and ~2010 cm^{-1} are observed,
462 together with a gradual decrease in ~2100 cm^{-1} intensity as CO reaches saturation. There is a rapid
463 decrease in intensity in the ~2100 cm^{-1} region and 2050 cm^{-1} region together with an increase in
464 2010 cm^{-1} region during the N_2 purging step. Overall, the results suggest that the nanoparticle
465 surfaces are largely made up of Cu sites, as expected for a dilute limit alloy. In this category of
466 isolated atom on a ultrasmall cluster of copper particle, the expected number of surface isolated
467 atoms for a diluted bimetallic would be small. Unlike the single atom alloy produced by the
468 galvanic displacement approach, the abundant base metal starts at a particle size with a significant
469 number of total atoms. The relatively large nanoparticles with several isolated atoms on the surface
470 may segrate once exposed to CO as presented by van Spronsen, M. A., et al. (2019) on a
471 Pd/Ag(111) system.[74] CO induced segration of surface atoms are also observed in moderate metal
472 ratio alloyed bimetallic catalysts and alloyed core-shell structure. [70,71] This state of segration is
473 believed to be not occurring in the current dilute limit alloy Pd-Cu catalysts prepared by co-SEA
474 with small size abundant metal.

475 The clearest comparison between monometallic Cu and the dilute limit alloys can be made by
476 considering the most strongly adsorbed species on each sample. Figure 8 shows the normalized (to

477 the ~2010 feature) final N_2-purged raw spectra for each DLA sample and for monometallic copper.
478 Once again, the overall similarity in the absorbance shape of these spectra is noted. However, two
479 regions (2000-2100 cm^{-1}, 1830-1940 cm^{-1}, highlighted in red) clearly show an added CO
480 absorbance that is absent from monometallic copper. These contributions to the spectra can be
481 attributed to the presence of Pd as either DLA sites or monometallic Pd.

482 Figure 9a shows the fitted spectra for monometallic 0.09 wt% Pd/SiO_2 (top) and 2.38 wt%
483 Cu/SiO_2 (bottom), and the most dilute Pd-Cu catalyst (middle). Deconvolution of DLA Pd-Cu
484 catalyst made use of the fitted Gaussian function parameters obtained from monometallic Cu
485 (green peaks). During fitting, the FWHM and peak positions of the Cu peaks were kept constant
486 while some peak ratios (minimal) and the overall intensity height were allowed to change. As can
487 be seen, there are no obvious features in the DLA that can be associated with monometallic Pd
488 (blue peaks). In order to fit the remaining spectral features, three new Gaussian peaks were
489 required. As seen more clearly in Figure 9b, a pair of linear CO peaks at 2046 and 2021 cm^{-1} were
490 found, with a single lower-frequency feature at 1908 cm^{-1} in the bridging region. Table S5 gives a
491 summary of Gaussian function parameters obtained during the fitting. It should be noted that these
492 three new peaks are present to varying extents in the other dilute limit alloy samples as shown in
493 Figure S7. In a study using Pd-Cu SAA nanoparticles with a particle size range from 3 to 7 nm, an
494 isolated peak at 2033 cm^{-1} associated with the linear CO on isolated Pd atom on copper was
495 observed. [9] In this study by Shan et al. (2020), the monometallic copper has no adsorption on the
496 2000 cm^{-1} region as compared with the current study. One possible explanation for this is the
497 significant difference in particle size. The SEA-derived catalysts explored here exhibit a Cu
498 particle size less than 1.5 nm, which high proportion of edge/step sites. In contrast, the catalysts
499 in Shan et al. (2020) ranged from 3-7 nm, which comprises mainly terrace sites. The electron

density on the copper surface is also dependent on the particle size as well as there possibly being a stronger metal-support interaction.

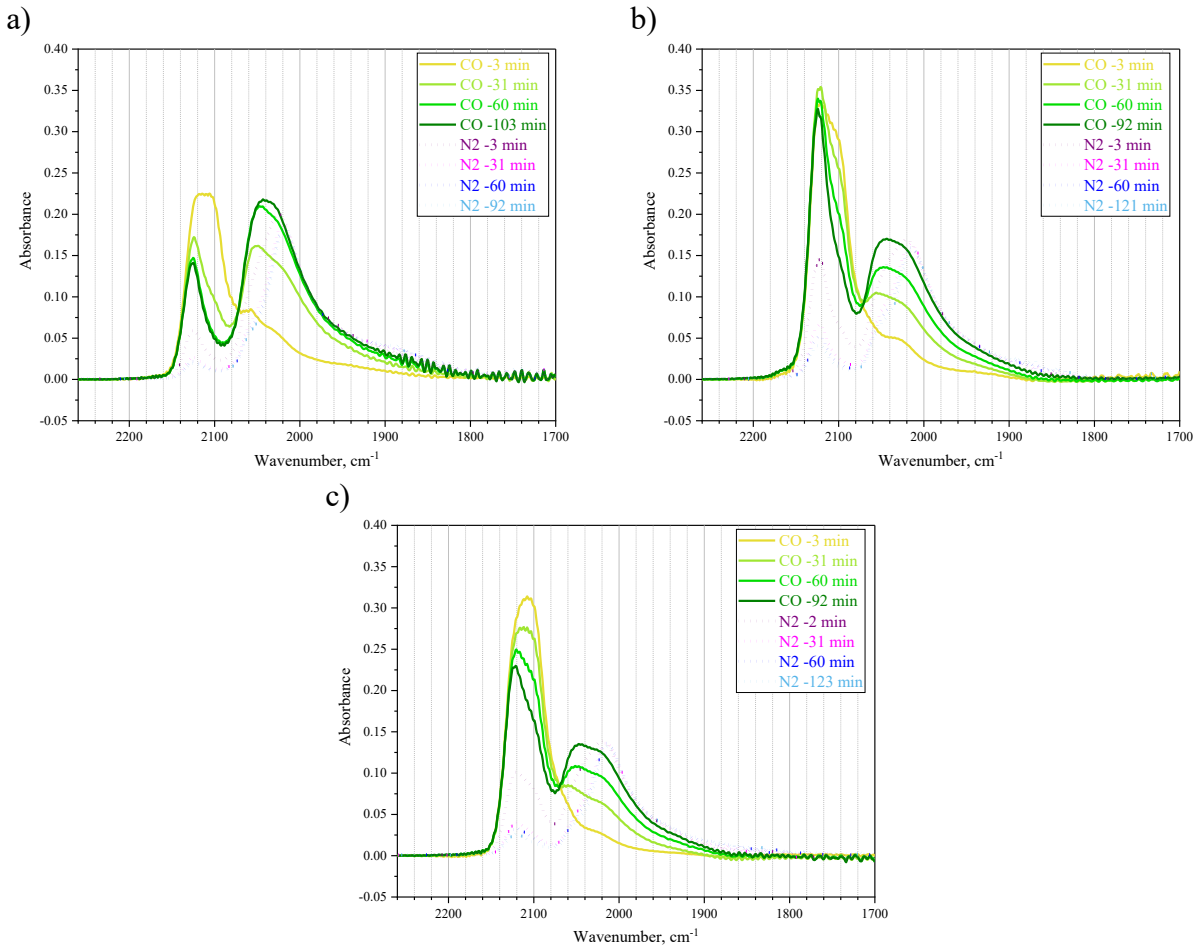

Figure 7. Selected blank-subtracted spectra for (a) 1/19, (b) 1/36 and (c) 1/74 Pd dilution on Cu.

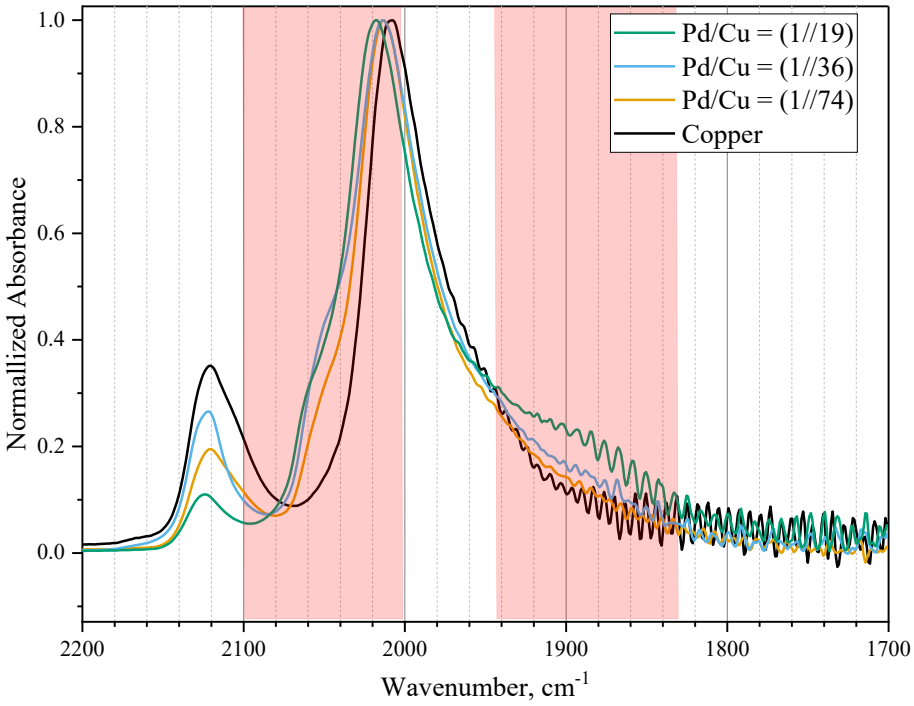

505

506 Figure 8. Normalized CO-FTIR spectra taken after 124 minutes of nitrogen purging for

507 monometallic copper and dilute limit alloy series Pd-Cu.

508 (a)

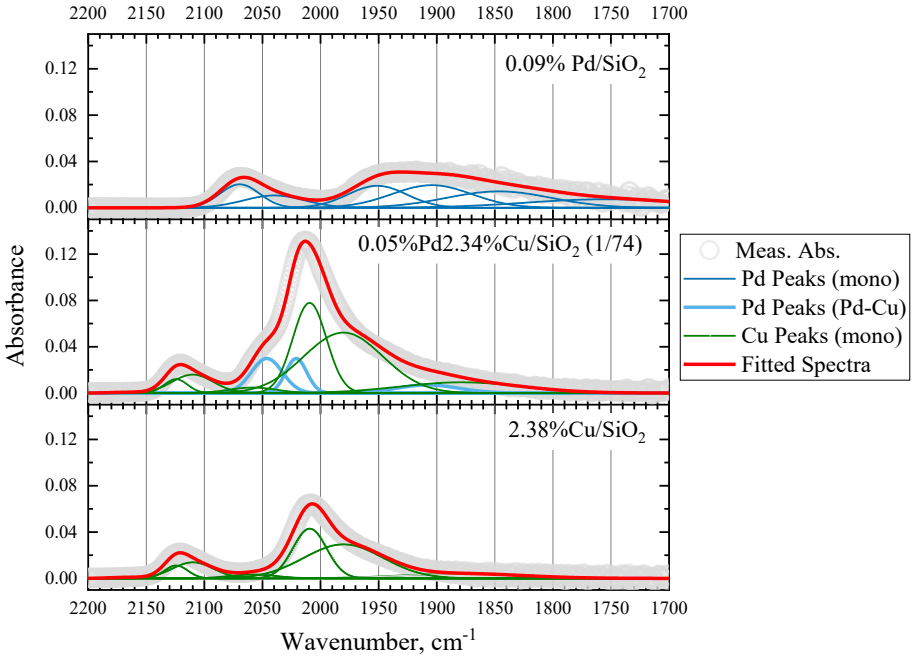

509

510 (b)

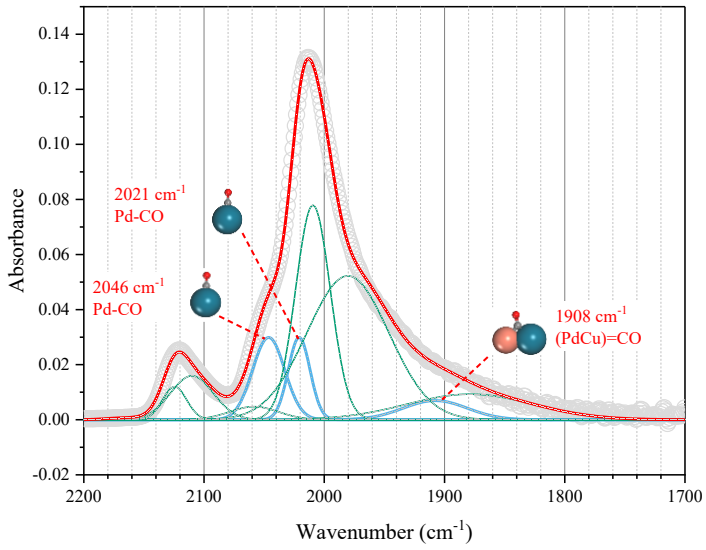

511

512 Figure 9. (a) Fitted spectra (final N_2 purged) for monometallic Pd and Cu, and bimetallic Pd-Cu

513 system and (b) three additional peak assignment for isolated palladium atom sites on Pd-Cu dilute

514 limit alloy.

3.3 DFT Calculation Results

DFT simulations were employed to assist in the band assignments of the three new peaks observed in the DLA samples as well as for the monometallic palladium and copper catalysts. Low coverage calculations were performed for four surface models (111, 100, 211 and 110) of monometallic palladium and copper surfaces and single atom alloy surfaces of bimetallic palladium-copper systems. Figure 10 and S4 illustrate the surface models and CO adsorption sites.

Table 4 shows the calculated wavenumber for adsorbed CO species on the various sites for the monometallic copper and palladium systems with the corresponding observed experimental CO-FTIR peaks. In all configurations, linearly adsorbed CO shows a wavenumber greater than 2000 cm^{-1}. The calculated wavenumbers for linearly adsorbed CO does not go beyond 2102 cm^{-1} (which we compute for a Cu adatom on Cu(111)). This conforms with the experimental results for monometallic palladium. For copper, the measured peak at 2124 cm^{-1} was assigned to a CO adsorbed linearly atop a Cu-adatom on the Cu(111) surface facet (Table 4). The DFT calculated wavenumber (2102 cm^{-1}) close to this value suggests a linear CO adsorbed on an undercoordinated copper adatom situated over a low index terrace site (although all Cu-adatom models display somewhat similar frequencies – Table 4).

DFT calculations also confirmed the presence of gem-carbonyl species where a $Cu(CO)_2$ complex was predicted to form over Cu(111) surface facets. The *gem*-dicarbonyl was oriented such that the (C-Cu-C) angle is 118.83° (Figure S8a & S8b). For the asymmetric stretching, we computed a frequency of 2064 cm^{-1} versus 2095 $cm^{-1}$for the symmetric stretching (Table 4)[93]. The difference of the calculated dicarbonyl wavenumbers (31cm^{-1}) is somewhat lower than that of the

experimental observation (52cm^{-1}); however, it is difficult to determine if this difference originates from computational uncertainties or the presence of another Cu site not investigated in this study.

For terrace surface facets, the calculated wavenumber for linear CO adsorbed on Cu(100) is greater than that of Cu (111) site, which implies a lesser degree of π-electron back donation on Cu(100). For copper, the degree of π backdonation is in direct correlation with the coordination number of the adsorption site with the fcc(111) surface atoms having CN=9 as compared with fcc(100) with CN=8. However, for monometallic palladium, the degree of π backdonation is lesser with increasing coordination number. This suggests that sharing of available electrons is dominating in palladium surface atoms. The higher coordination number of Pd (111) terrace sites as compared with Pd (100) shows a higher wavenumber, which implies less available electrons for π backdonation. With respect to the number of metal atoms coordinated with the adsorbed CO, the calculated frequency obeys the trend as atop > bridge > 3-fold-hollow > 4-fold-hollow.

Table 5 shows the calculated frequencies for CO adsorbed on isolated palladium on four types of copper surface facets with an embedded and ad-atom configuration (Figure 10 & 12). From the experimental CO vibration results for the isolated Pd, the association with the calculated wavenumbers was made accordingly. For a linearly adsorbed CO on an isolated palladium atom, a wavenumber of 2052 cm^{-1} was calculated for atop CO on Pd embedded on a Cu(100) facet (Figure 10e). Within the range of computation certainty, vibration frequencies for CO adsorbed on Pd adatoms on Cu(100) (2052 cm^{-1}), Cu(111) (2058 cm^{-1}) and Cu(211) (2048 cm^{-1}) were also calculated (Table 5). A significantly lower wavenumber at 2026 cm^{-1} was obtained for Pd single-atoms embedded in a Cu(111) facet (Figure 10c). The trend in CO frequency can be explained by the Dewar–Chatt–Duncanson (DCD) model.[94] With copper acting as a ligand that donates electrons to the isolated palladium atom, as the coordination number of Pd with Cu increases, the

number of electrons available for backdonation also increases giving a much lower CO wavenumber. DFT calculated a 1911 cm^{-1} frequency on CO forming a bridge between Pd and Cu on a Pd embedded on a Cu(211) terrace site. This frequency is within the region of the additional bridge peak that was required to fit the spectra for the Pd-Cu DLA (1908 cm^{-1}). As the particle gets smaller, the percentage of undercoordinated atoms such as, e.g. edges and steps, increases relative to terrace surface atoms. The Benfield (1992) model on cuboctahedral cluster particles suggests that as the particle size falls below 2 nm the fraction of edge atoms can go beyond 50%.[37] Given this surface atom distribution, there is a high probability of this isolated Pd atom situated on step-edge sites of the abundant metal. For clusters, geometrical factors could change, such as a shorter span of the terrace facet making no significant difference in (111) and (100) facets CO adsorption.

572 Table 4. DFT calculation on CO vibration frequency for the monometallic copper and palladium
573 systems. If the adsorption site is not located at a potential energy minimum, it is considered
574 unstable and hence no frequency was calculated. Figure S8 & S9 lists all the adsorption sites for
575 the monometallic systems.

System	Adsorption Site	C-O stretching frequency (cm^{-1})			
		Copper		Palladium	
		Calculated	Observed (range)	Calculated	Observed (range)
(100)	atop (a)	2052	2050 to 2058	2057	2038 to 2047
	bridge (b)	1913		1890	
	4-fold-hollow (4f)	1727		1756	1755
(110)	atop (a)	2061	2050 to 2058	2050	2038 to 2047
	terrace bridge (tb)	1931		1822	
	step bridge (sb)	1928		1881	
(111)	atop (a)	2017	2009	2072	2069 to 2086
	Bridge (b)	1853	1879	1882	
	fcc, hcp	1855	1879	1801	
(211)	atop step (ts)	2064	2050 to 2058	2054	2038 to 2047
	atop terrace (tt)	2038		unstable	
	step bridge (eb)	unstable		1893	1904
	step-terrace bridge (sb1)	unstable		unstable	
	step-terrace bridge (sb2)	1915		1873	
	3-fold-hollow (h)	1828		1725	1755
	3-fold hollow (f1)	1802		1794	1755
Cu-adatom /Cu(111)	$Cu(CO)_1$	2102	2124	NA	
	$Cu(CO)_2$	2064,2095	(2050 to 2058, 2104 to 2110)	NA	
Cu-adatom /Cu(211)	$Cu(CO)_1$	2097		NA	
	$Cu(CO)_2$	2037,2074		NA	
Cu-adatom /Cu(110)	$Cu(CO)_1$	2084		NA	
Cu-adatom /Cu(100)	$Cu(CO)_1$	2084		NA	

576

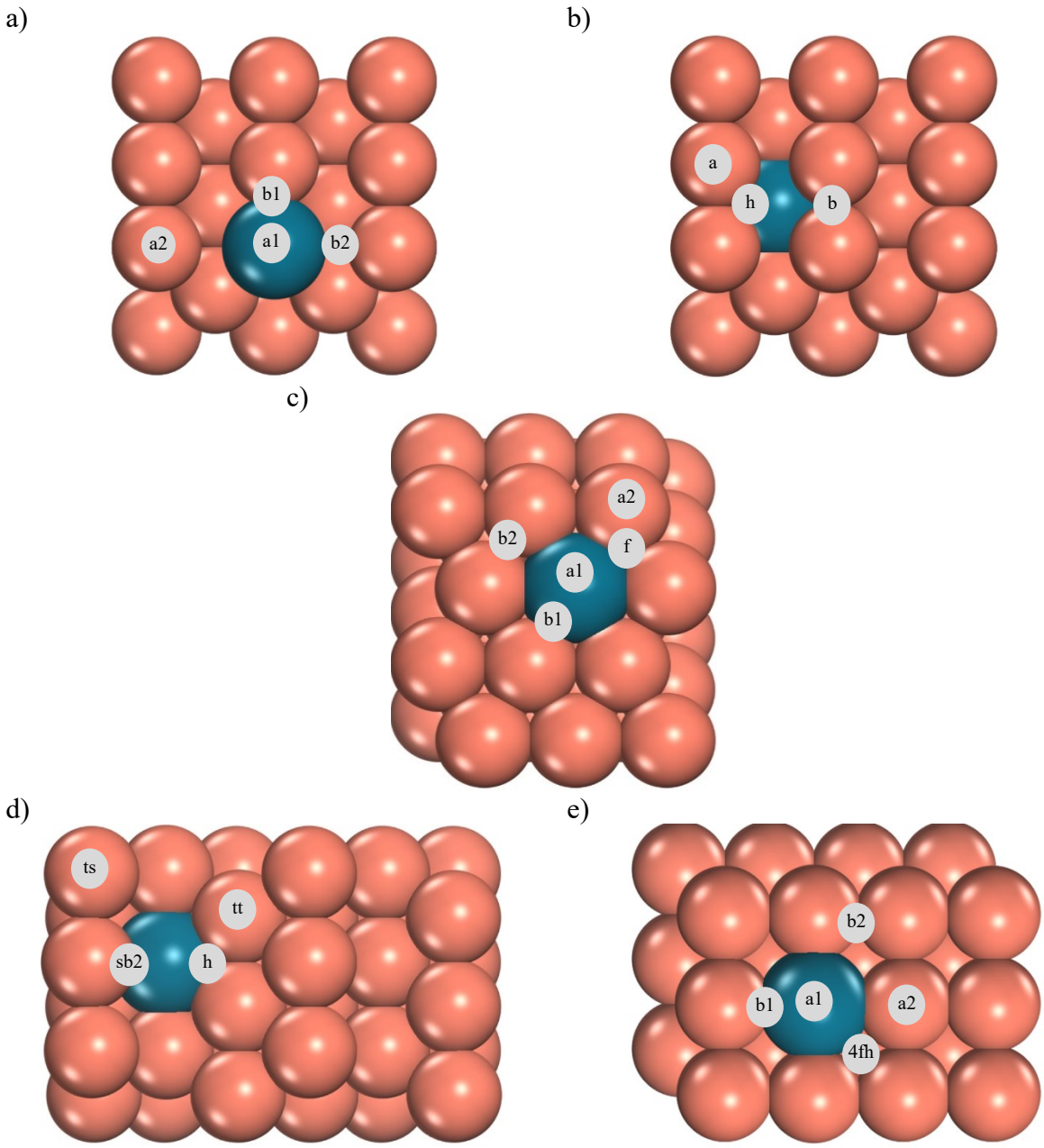

577 Figure 10. Stable adsorption sites for Pd-Cu bimetallic catalyst. a) Cu(110) facet alloyed with a Pd
578 atom replacing a step Cu atom, b) Cu(110) facet alloyed with a Pd atom replacing a terrace Cu
579 atom, c) Cu(111) facet alloyed with a Pd atom (Pd/Cu111), d) Cu(211) facet alloyed with a Pd
580 atom (Pd/Cu211) where the Pd atom has a coordination number (CN) of 10, and e) Cu(100) facet
581 alloyed with a Pd atom (Pd/Cu100).

582 Table 5. DFT calculation on CO vibration frequency for the dilute limit alloy bimetallic palladium-

583 copper system.

System	Adsorption Site	C-O stretching frequency (cm^{-1})	
		DFT Calculated	Observed (Pd)
Pd/Cu(100)	atop-Pd (a1)	2052	2046
	atop-Cu (a2)	1928	
	Pd-Cu bridge (b1)	1930	
	Cu-Cu bridge (b2)	1914	
	hollow (4-fold)	1927	
Pd/Cu(111)	atop-Pd (a1)	2026	2021
	atop-Cu (a2)	2057	
	Pd-Cu bridge (b1)	1927	
	Cu-Cu bridge (b2)	1865	
	2Cu-1Pd-FCC (F)	1873	
Pd/Cu(211)	3-fold-hollow (h)	1852	
	Pd-Cu step-terrace bridge (sb2)	1911	1908
	atop-Cu step (ts)	2066	
	Atop-Cu terrace (tt)	2044	
Pd/Cu(110) (Pd in step)	atop-Pd (a1)	2046	
	atop-Cu (a2)	2061	
	2-step bridge Pd-Cu (b2)	1882	
	1-step bridge Pd-Cu (b1)	1934	
Pd/Cu(110) (Pd in terrace)	atop-Cu (a)	2063	
	bridge-Cu-Cu (b)	1932	
	3-fold-hollow (h)	1822	
Pd-adatom/Cu(100)	atop-Pd	2052	2046
Pd-adatom/Cu(111)	atop-Pd	2059	2046
Pd-adatom/Cu(211)	atop-Pd	2048	2046

584

585

586

a)

b)

c)

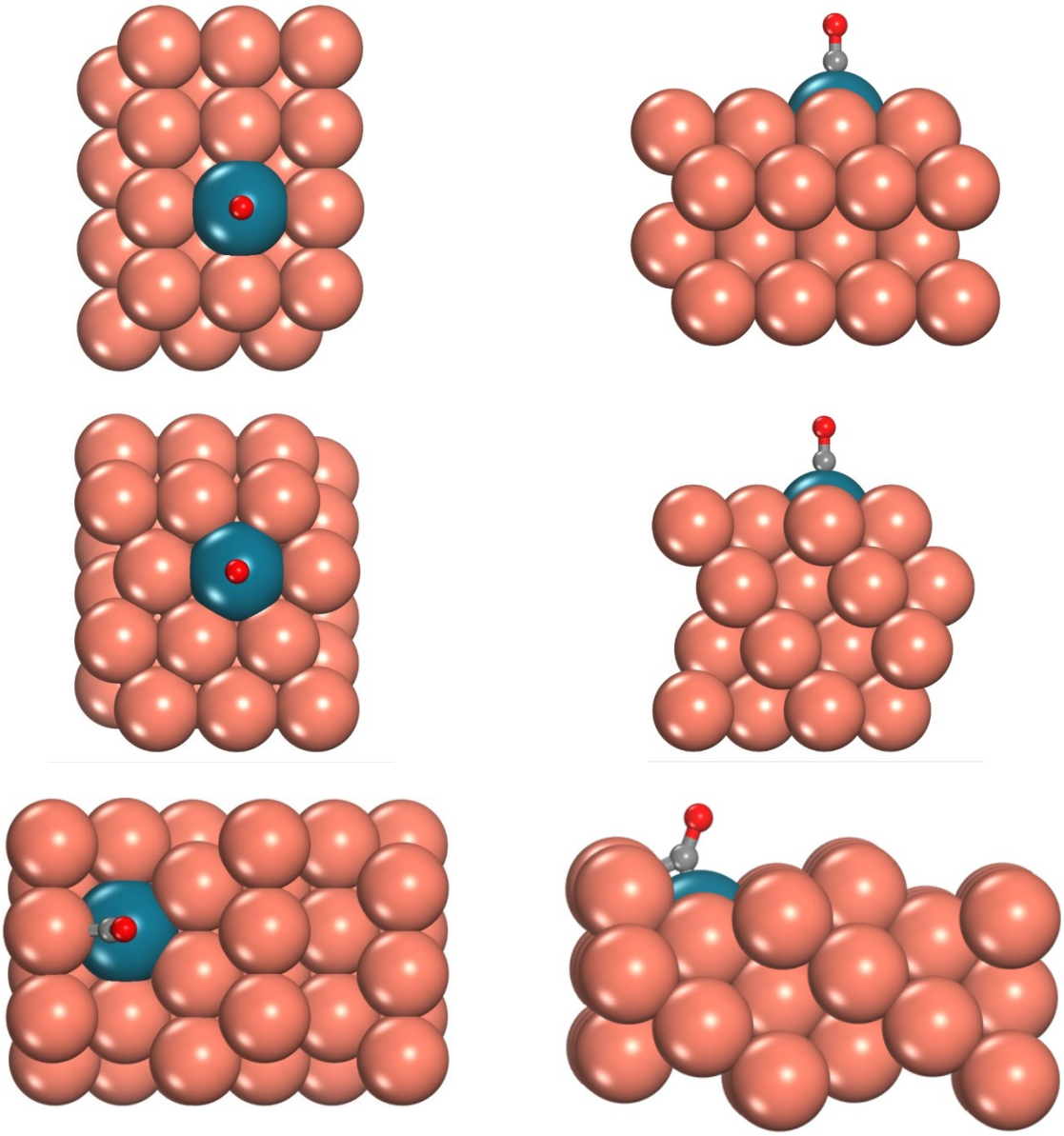

Figure 11. Top and side views of surface models corresponding to experimentally observed CO vibration; (a) 2052 cm^{-1} atop CO on Pd/Cu(100), (b) 2026 cm^{-1} atop CO on Pd/Cu(111), and (c) 1911 cm^{-1} bridge CO.

590

a) b)

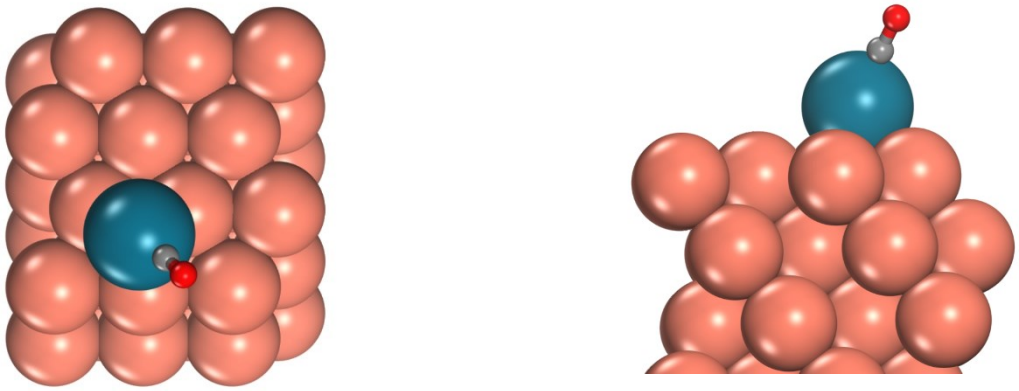

c) d)

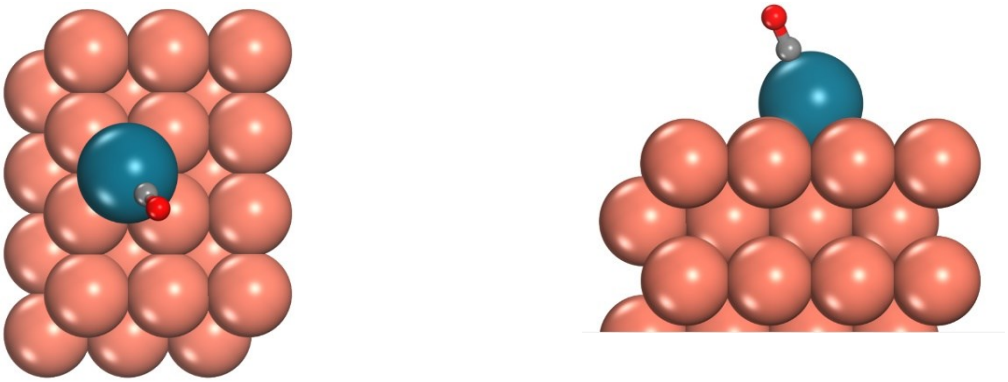

e) f)

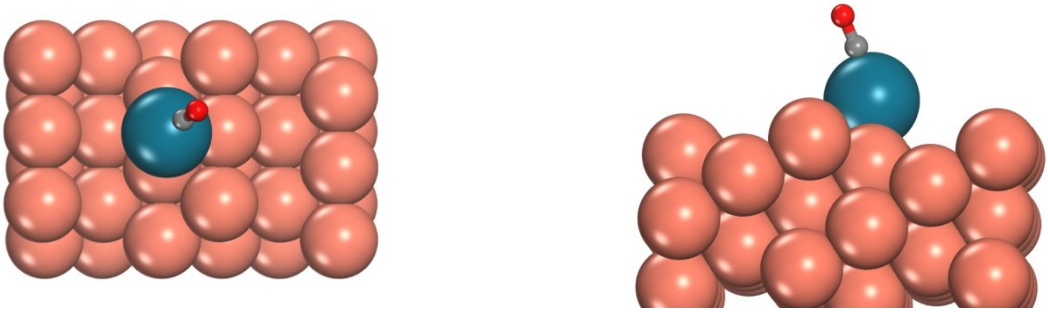

591 Figure 12.Top and side views of surface models of Pd-adatom with CO vibrations;(a,b) 2059 cm-

592 [1] on Cu(111),(c,d) 2052 cm^{-1} on Cu(100), and (e,f) 2048 cm^{-1} on Cu(211) .

593

594

595

4. Conclusions

A facile synthesis method to prepare DLAs of Pd in Cu supported on SiO_2 has been demonstrated. Simultaneous co-SEA combined with controlled removal of ligands and reduction of the metal resulted in the formation of small metallic clusters on the support surface. These reduced particles presented isolated Pd sites on their surface, as confirmed by in-situ FTIR spectroscopy measurements of adsorbed CO and complementary DFT computations. In addition, at the low dilution levels examined, no evidence could be found for formation of monometallic clusters or particles of Pd.

The present results suggest that co-SEA can provide a more general and scalable approach to producing highly dispersed DLA catalysts as compared with other more exotic approaches. While only Pd and Cu are considered here, SEA is applicable to the entire range of transition metals relevant to catalysis. In the present case, Pd was found to situate itself on the Cu surface, or at least be drawn out to the surface during CO adsorption. However, depending on the metals in question, a dilute species might be submerged within the other metal. Ongoing studies in our laboratory are exploring these Pd-Cu and other co-SEA-derived DLA catalysts for a variety of catalytic applications, including selective hydrogenation reactions.

5. Supporting Information

Supporting raw CO-FTIR spectra, STEM images, fitted Gaussian functions parameters, additional DFT models and XPS spectra are available in the supplementary material.

6 Acknowledgments

D.S. and A.H. acknowledge financial support from the National Science Foundation under Grant No. CBET-1805307 and the South Carolina State Center for Strategic Approaches to the Generation of Electricity (SAGE). Computing resources have been provided by the National Energy Research Scientific Computing Center (NERSC) under Contract No. DE-AC02-

620 05CH11231 and Pacific Northwest National Laboratory (Ringgold ID 130367, Grant Proposal
621 51711), XSEDE facilities located at San Diego Supercomputer Center (SDSC) and Texas
622 advanced Computing Center (TACC) under grant number TG-CTS090100, and the High-
623 Performance Computing clusters located at University of South Carolina.

624 L.D. , C.W., and J.R. acknowledge financial support from Catalysis for Renewable Fuels Center
625 (CReF), University of South Carolina. We also acknowledge the XPS measurements made by Dr.
626 Stavros Karakalos and the STEM images captured by Dr. Abolfazl Sahkouri.

627 L.D. also acknowledges the financial support from Engineering Research Development for
628 Technology (ERDT), Department of Science and Technology (DOST), Republic of the Philippines
629 under the Engineering R&D for Technology Faculty Development Foreign PhD Scholarship
630 Grant.

631

632

633

634

635

636

637

638

7. References

(1) Thomas, J. M.; Harris, K. D. M. Some of Tomorrow's Catalysts for Processing Renewable and Non-Renewable Feedstocks, Diminishing Anthropogenic Carbon Dioxide and Increasing the Production of Energy. *Energy Environ. Sci.* **2016**, *9* (3), 687–708. https://doi.org/10.1039/c5ee03461b.

(2) Thomas, J. M.; Raja, R. The Advantages and Future Potential of Single-Site Heterogeneous Catalysts. *Top. Catal.* **2006**, *40* (1–4), 3–17. https://doi.org/10.1007/s11244-006-0105-7.

(3) Fu, Q.; Saltsburg, H.; Flytzani-Stephanopoulos, M. Active Nonmetallic Au and Pt Species on Ceria-Based Water-Gas Shift Catalysts. *Science (80-.).* **2003**, *301* (5635), 935–938. https://doi.org/10.1126/science.1085721.

(4) Darby, M. T.; Stamatakis, M.; Michaelides, A.; Sykes, E. C. H. Lonely Atoms with Special Gifts: Breaking Linear Scaling Relationships in Heterogeneous Catalysis with Single-Atom Alloys. *Journal of Physical Chemistry Letters*. American Chemical Society September 2018, pp 5636–5646. https://doi.org/10.1021/acs.jpclett.8b01888.

(5) Hannagan, R. T.; Giannakakis, G.; Flytzani-Stephanopoulos, M.; Sykes, E. C. H. Single-Atom Alloy Catalysis. *Chem. Rev.* **2020**, *120* (21), 12044–12088. https://doi.org/10.1021/acs.chemrev.0c00078.

(6) Thomas, J. M.; Raja, R.; Lewis, D. W. Single-Site Heterogeneous Catalysts. *Angew. Chemie - Int. Ed.* **2005**, *44* (40), 6456–6482. https://doi.org/10.1002/anie.200462473.

(7) Cao, X.; Fu, Q.; Luo, Y. Catalytic Activity of Pd-Doped Cu Nanoparticles for Hydrogenation as a Single-Atom-Alloy Catalyst. *Phys. Chem. Chem. Phys.* **2014**, *16* (18),

8367–8375. https://doi.org/10.1039/c4cp00399c.

(8) Boucher, M. B.; Zugic, B.; Cladaras, G.; Kammert, J.; Marcinkowski, M. D.; Lawton, T. J.; Sykes, E. C. H.; Flytzani-Stephanopoulos, M. Single Atom Alloy Surface Analogs in Pd0.18Cu15 Nanoparticles for Selective Hydrogenation Reactions. *Phys. Chem. Chem. Phys.* **2013**, *15* (29), 12187–12196. https://doi.org/10.1039/c3cp51538a.

(9) Shan, J.; Giannakakis, G.; Liu, J.; Cao, S.; Ouyang, M.; Li, M.; Lee, S.; Flytzani-Stephanopoulos, M. PdCu Single Atom Alloys for the Selective Oxidation of Methanol to Methyl Formate at Low Temperatures. *Top. Catal.* **2020**, *63* (7–8), 618–627. https://doi.org/10.1007/s11244-020-01288-x.

(10) Trimpalis, A.; Giannakakis, G.; Cao, S.; Flytzani-Stephanopoulos, M. NiAu Single Atom Alloys for the Selective Oxidation of Methacrolein with Methanol to Methyl Methacrylate. *Catal. Today* **2019**. https://doi.org/10.1016/J.CATTOD.2019.04.021.

(11) Shan, J.; Liu, J.; Li, M.; Lustig, S.; Lee, S.; Flytzani-Stephanopoulos, M. NiCu Single Atom Alloys Catalyze the CH Bond Activation in the Selective Non- Oxidative Ethanol Dehydrogenation Reaction. *Appl. Catal. B Environ.* **2018**, *226*, 534–543. https://doi.org/10.1016/J.APCATB.2017.12.059.

(12) Lucci, F. R.; Liu, J.; Marcinkowski, M. D.; Yang, M.; Allard, L. F.; Flytzani-Stephanopoulos, M.; Sykes, E. C. H. Selective Hydrogenation of 1,3-Butadiene on Platinum-Copper Alloys at the Single-Atom Limit. *Nat. Commun.* **2015**, *6*, 1–8. https://doi.org/10.1038/ncomms9550.

(13) Zhang, Y.; Diao, W.; Monnier, J. R.; Williams, C. T. Pd-Ag/SiO2 Bimetallic Catalysts

Prepared by Galvanic Displacement for Selective Hydrogenation of Acetylene in Excess Ethylene. *Catal. Sci. Technol.* **2015**, *5* (8), 4123–4132. https://doi.org/10.1039/c5cy00353a.

(14) Zhang, X.; Cui, G.; Feng, H.; Chen, L.; Wang, H.; Wang, B.; Zhang, X.; Zheng, L.; Hong, S.; Wei, M. Platinum–Copper Single Atom Alloy Catalysts with High Performance towards Glycerol Hydrogenolysis. *Nat. Commun.* **2019**, *10* (1), 1–12. https://doi.org/10.1038/s41467-019-13685-2.

(15) Liu, J.; Shan, J.; Lucci, F. R.; Cao, S.; Sykes, E. C. H.; Flytzani-Stephanopoulos, M. Palladium-Gold Single Atom Alloy Catalysts for Liquid Phase Selective Hydrogenation of 1-Hexyne. *Catal. Sci. Technol.* **2017**, *7* (19), 4276–4284. https://doi.org/10.1039/c7cy00794a.

(16) Chen, C. H.; Wu, D.; Li, Z.; Zhang, R.; Kuai, C. G.; Zhao, X. R.; Dong, C. K.; Qiao, S. Z.; Liu, H.; Du, X. W. Ruthenium-Based Single-Atom Alloy with High Electrocatalytic Activity for Hydrogen Evolution. *Adv. Energy Mater.* **2019**, *9* (20), 1–7. https://doi.org/10.1002/aenm.201803913.

(17) Degnan, T. Single-Atom Catalysis – the Future Looks Bright. *Focus Catal.* **2016**, *2016* (11), 1–2. https://doi.org/10.1016/J.FOCAT.2016.10.001.

(18) Thirumalai, H.; Kitchin, J. R. Investigating the Reactivity of Single Atom Alloys Using Density Functional Theory. *Top. Catal.* **2018**, *61* (5–6), 462–474. https://doi.org/10.1007/s11244-018-0899-0.

(19) Zhang, Y.; Shi, X. R.; Sun, C.; Huang, S.; Duan, Z.; Ma, P.; Wang, J. CO Oxidation on Ni-Based Single-Atom Alloys Surfaces. *Mol. Catal.* **2020**, *495* (July), 111154.

https://doi.org/10.1016/j.mcat.2020.111154.

(20) Shan, J.; Janvelyan, N.; Li, H.; Liu, J.; Egle, T. M.; Ye, J.; Biener, M. M.; Biener, J.; Friend, C. M.; Flytzani-Stephanopoulos, M. Selective Non-Oxidative Dehydrogenation of Ethanol to Acetaldehyde and Hydrogen on Highly Dilute NiCu Alloys. *Appl. Catal. B Environ.* **2017**, *205*, 541–550. https://doi.org/10.1016/J.APCATB.2016.12.045.

(21) Marcinkowski, M. D.; Darby, M. T.; Liu, J.; Wimble, J. M.; Lucci, F. R.; Lee, S.; Michaelides, A.; Flytzani-Stephanopoulos, M.; Stamatakis, M.; Sykes, E. C. H. Pt/Cu Single-Atom Alloys as Coke-Resistant Catalysts for Efficient C-H Activation. *Nat. Chem.* **2018**, *10* (3), 325–332. https://doi.org/10.1038/NCHEM.2915.

(22) Nguyen, L.; Zhang, S.; Tan, L.; Tang, Y.; Liu, J.; Tao, F. F. Ir1Zn n Bimetallic Site for Efficient Production of Hydrogen from Methanol. *ACS Sustain. Chem. Eng.* **2019**, *7* (23), 18793–18800. https://doi.org/10.1021/acssuschemeng.9b03247.

(23) Zhang, S.; Nguyen, L.; Liang, J. X.; Shan, J.; Liu, J. J.; Frenkel, A. I.; Patlolla, A.; Huang, W.; Li, J.; Tao, F. F. Catalysis on Singly Dispersed Bimetallic Sites. *Nat. Commun.* **2015**, *6*, 1–10. https://doi.org/10.1038/ncomms8938.

(24) Lu, J.; Low, K. Bin; Lei, Y.; Libera, J. A.; Nicholls, A.; Stair, P. C.; Elam, J. W. Toward Atomically-Precise Synthesis of Supported Bimetallic Nanoparticles Using Atomic Layer Deposition. *Nat. Commun.* **2014**, *5*. https://doi.org/10.1038/ncomms4264.

(25) Zhang, L.; Ball, M. R.; Liu, Y.; Kuech, T. F.; Huber, G. W.; Mavrikakis, M.; Hermans, I.; Dumesic, J. A. Synthesis Gas Conversion over Rh/Mo Catalysts Prepared by Atomic Layer Deposition. **2019**. https://doi.org/10.1021/acscatal.8b04649.

(26) Ramachandran, R. K.; Dendooven, J.; Detavernier, C. Controlled Synthesis of Fe-Pt Nanoalloys Using Atomic Layer Deposition. *Nanotechnology* **2021**, *32* (9). https://doi.org/10.1088/1361-6528/abc5f5.

(27) Ingale, P.; Knemeyer, K.; Preikschas, P.; Ye, M.; Geske, M.; Naumann d'Alnoncourt, R.; Thomas, A.; Rosowski, F. Design of PtZn Nanoalloy Catalysts for Propane Dehydrogenation through Interface Tailoringviaatomic Layer Deposition. *Catal. Sci. Technol.* **2021**, *11* (2), 484–493. https://doi.org/10.1039/d0cy01528h.

(28) Wang, H.; Luo, Q.; Liu, W.; Lin, Y.; Guan, Q.; Zheng, X.; Pan, H.; Zhu, J.; Sun, Z.; Wei, S.; et al. Quasi Pd1Ni Single-Atom Surface Alloy Catalyst Enables Hydrogenation of Nitriles to Secondary Amines. *Nat. Commun.* **2019**, *10* (1), 1–9. https://doi.org/10.1038/s41467-019-12993-x.

(29) Filie, A.; Shirman, T.; Aizenberg, M.; Aizenberg, J.; Friend, C. M.; Madix, R. J. The Dynamic Behavior of Dilute Metallic Alloy PdxAu1−x/SiO2raspberry Colloid Templated Catalysts under CO Oxidation. *Catal. Sci. Technol.* **2021**, *11* (12), 4072–4082. https://doi.org/10.1039/d1cy00469g.

(30) Sun, G.; Zhao, Z. J.; Mu, R.; Zha, S.; Li, L.; Chen, S.; Zang, K.; Luo, J.; Li, Z.; Purdy, S. C.; et al. Breaking the Scaling Relationship via Thermally Stable Pt/Cu Single Atom Alloys for Catalytic Dehydrogenation. *Nat. Commun.* **2018**, *9* (1). https://doi.org/10.1038/s41467-018-06967-8.

(31) Ma, L.; Jia, I.; Guo, X.; Xiang, L. High Performance of Pd Catalysts on Bimodal Mesopore for the Silica Catalytic Oxidation of Toluene. *Chinese J. Catal.* **2014**, *35* (0), 108–119.

https://doi.org/10.1016/S1872.

(32) Pei, G. X.; Liu, X. Y.; Wang, A.; Lee, A. F.; Isaacs, M. A.; Li, L.; Pan, X.; Yang, X.; Wang, X.; Tai, Z.; et al. Ag Alloyed Pd Single-Atom Catalysts for Efficient Selective Hydrogenation of Acetylene to Ethylene in Excess Ethylene. *ACS Catal.* **2015**, *5* (6), 3717–3725. https://doi.org/10.1021/acscatal.5b00700.

(33) Xing, F.; Jeon, J.; Toyao, T.; Shimizu, K. I.; Furukawa, S. A Cu-Pd Single-Atom Alloy Catalyst for Highly Efficient NO Reduction. *Chem. Sci.* **2019**, *10* (36), 8292–8298. https://doi.org/10.1039/c9sc03172c.

(34) Rassolov, A. V.; Bragina, G. O.; Baeva, G. N.; Smirnova, N. S.; Kazakov, A. V.; Mashkovsky, I. S.; Bukhtiyarov, A. V.; Zubavichus, Y. V.; Stakheev, A. Y. Formation of Isolated Single-Atom Pd1 Sites on the Surface of Pd–Ag/Al2O3 Bimetallic Catalysts. *Kinet. Catal.* **2020**, *61* (5), 758–767. https://doi.org/10.1134/S0023158420050080.

(35) Yang, C.; Miao, Z.; Zhang, F.; Li, L.; Liu, Y.; Wang, A.; Zhang, T. Hydrogenolysis of Methyl Glycolate to Ethanol over a Pt–Cu/SiO2 Single-Atom Alloy Catalyst: A Further Step from Cellulose to Ethanol. *Green Chem.* **2018**, *20* (9), 2142–2150. https://doi.org/10.1039/c8gc00309b.

(36) Aich, P.; Wei, H.; Basan, B.; Kropf, A. J.; Schweitzer, N. M.; Marshall, C. L.; Miller, J. T.; Meyer, R. Single-Atom Alloy Pd-Ag Catalyst for Selective Hydrogenation of Acrolein. *J. Phys. Chem. C* **2015**, *119* (32), 18140–18148. https://doi.org/10.1021/acs.jpcc.5b01357.

(37) Benfield, R. E. Mean Coordination Numbers and the Non-Metal-Metal Transition in Clusters. **1992**, *88* (8), 1107–1110.

(38) Cho, H. R.; Regalbuto, J. R. The Rational Synthesis of Pt-Pd Bimetallic Catalysts by Electrostatic Adsorption. *Catal. Today* **2015**, *246*, 143–153. https://doi.org/10.1016/j.cattod.2014.09.029.

(39) Simonovis, J. P.; Hunt, A.; Palomino, R. M.; Senanayake, S. D.; Waluyo, I. Enhanced Stability of Pt-Cu Single-Atom Alloy Catalysts: In Situ Characterization of the Pt/Cu(111) Surface in an Ambient Pressure of CO. *J. Phys. Chem. C* **2018**, *122* (8). https://doi.org/10.1021/acs.jpcc.8b00078.

(40) Datye, A. K.; Guo, H. Single Atom Catalysis Poised to Transition from an Academic Curiosity to an Industrially Relevant Technology. *Nat. Commun.* **2021**, *12* (1), 10–12. https://doi.org/10.1038/s41467-021-21152-0.

(41) Wong, A.; Liu, Q.; Griffin, S.; Nicholls, A.; Regalbuto, J. R. Synthesis of Ultrasmall, Homogeneously Alloyed, Bimetallic Nanoparticles on Silica Supports. *Science (80-.).* **2017**, *358* (6369), 1427–1430. https://doi.org/10.1126/science.aao6538.

(42) Jiao, L.; Regalbuto, J. R. The Synthesis of Highly Dispersed Noble and Base Metals on Silica via Strong Electrostatic Adsorption: I. Amorphous Silica. *J. Catal.* **2008**, *260* (2), 329–341. https://doi.org/10.1016/j.jcat.2008.09.023.

(43) Sheppard, N.; De La Cruz, C. The Reliability of Vibrational Spectroscopy as a Means of Identification of the Structures of Chemisorbed Species on Metal Surfaces: The Cases of CO, NO and C2 Hydrocarbon Surface Species. *Catal. Today* **2001**, *70* (1–3), 3–13. https://doi.org/10.1016/S0920-5861(01)00403-5.

(44) Chin, S. Y.; Williams, C. T.; Amiridis, M. D. FTIR Studies of CO Adsorption on Al2O3-

and SiO 2-Supported Ru Catalysts. *J. Phys. Chem. B* **2006**, *110* (2), 871–882. https://doi.org/10.1021/jp053908q.

(45) Rebelli, J.; Rodriguez, A. A.; Ma, S.; Williams, C. T.; Monnier, J. R. Preparation and Characterization of Silica-Supported, Group IB–Pd Bimetallic Catalysts Prepared by Electroless Deposition Methods. *Catal. Today* **2011**, *160* (1), 170–178. https://doi.org/10.1016/J.CATTOD.2010.06.011.

(46) Jiao, L.; Regalbuto, J. R. The Synthesis of Highly Dispersed Noble and Base Metals on Silica via Strong Electrostatic Adsorption: II. Mesoporous Silica SBA-15. *J. Catal.* **2008**, *260* (2), 342–350. https://doi.org/10.1016/j.jcat.2008.09.023.

(47) Wojdyr, M. Fityk: A General-Purpose Peak Fitting Program. *J. Appl. Crystallogr.* **2010**, *43* (5 PART 1), 1126–1128. https://doi.org/10.1107/S0021889810030499.

(48) Kresse, G.; Furthmüller, J. Efficiency of Ab-Initio Total Energy Calculations for Metals and Semiconductors Using a Plane-Wave Basis Set. *Comput. Mater. Sci.* **1996**, *6* (1), 15–50. https://doi.org/10.1016/0927-0256(96)00008-0.

(49) Kresse, G.; Hafner, J. Ab Initio Molecular Dynamcis for Liquid Metals. *Phys. Rev. B* **1993**, *47* (1), 558.

(50) Kresse, G.; Joubert, D. Kresse, Joubert - Unknown - From Ultrasoft Pseudopotentials to the Projector Augmented-Wave Method. **1999**, *59* (3), 11–19.

(51) Hammer, B.; Hansen, L. B.; No, J. K. Improved Adsorption Energetics within Density-Functional Theory Using Revised Perdew-Burke-Ernzerhof Functionals. **1999**, *59* (11), 7413–7421.

(52) Feibelman, P. J.; Hammer, B.; Wagner, F.; Scheffler, M.; Stumpf, R.; Watwe, R.; Dumesic, J. The CO / Pt (111) Puzzle †. **2001**, No. 111, 4018–4025.

(53) Eichler, A.; Hafner, J. CO Adsorption on Cu(211) Surface: First Principle and STM Study. **2004**, No. April.

(54) Gajdos, M. CO Adsorption on Cu (1 1 1) and Cu (0 0 1) Surfaces : Improving Site Preference in DFT Calculations. **2005**, *590*, 117–126. https://doi.org/10.1016/j.susc.2005.04.047.

(55) Gameel, K. M.; Sharafeldin, I. M.; Abourayya, A. U.; Biby, A. H. Unveiling CO Adsorption on Cu Surfaces : New Insights from Molecular Orbital Principles †. **2018**, 25892–25900. https://doi.org/10.1039/c8cp04253e.

(56) Harris, J. Simplified Method for Calculating the Energy of Weakly Interacting Fragments. *Phys. Rev. B* **1985**, *31* (4), 1770–1779. https://doi.org/10.1103/PhysRevB.31.1770.

(57) Foulkes, W. M. C.; Haydock, R. Tight-Binding Models and Density-Functional Theory. *Phys. Rev. B* **1989**, *39* (17), 12520–12536. https://doi.org/10.1103/PhysRevB.39.12520.

(58) Makov, G.; Payne, M. C. Periodic Boundary Conditions in Ab Initio Calculations. *Phys. Rev. B* **1995**, *51* (7), 4014–4022. https://doi.org/10.1103/PhysRevB.51.4014.

(59) Pack, J. D.; Monkhorst, H. J. "special Points for Brillouin-Zone Integrations"-a Reply. *Phys. Rev. B* **1977**, *16* (4), 1748–1749. https://doi.org/10.1103/PhysRevB.16.1748.

(60) Methfessel, M.; Paxton, A. T. High-Precision Sampling for Brillouin-Zone Integration in Metals. *Phys. Rev. B* **1989**, *40* (6), 3616–3621. https://doi.org/10.1103/PhysRevB.40.3616.

(61) Davey, W. P. Precision Measurements of the Lattice Constants of Twelve Common Metals. *Phys. Rev.* **1925**, *538* (1922), 735–761. https://doi.org/10.1103/PhysRev.25.753.

(62) Henkelman, G.; Uberuaga, B. P.; Jónsson, H. Climbing Image Nudged Elastic Band Method for Finding Saddle Points and Minimum Energy Paths. *J. Chem. Phys.* **2000**, *113* (22), 9901–9904. https://doi.org/10.1063/1.1329672.

(63) Laury, M. L.; Carlson, M. J.; Wilson, A. K. Vibrational Frequency Scale Factors for Density Functional Theory and the Polarization Consistent Basis Sets. **2012**. https://doi.org/10.1002/jcc.23073.

(64) Martin, N. M.; Bossche, M. Van Den; Gro, H.; Hakanoglu, C.; Zhang, F.; Li, T.; Gustafson, J.; Weaver, J. F.; Lundgren, E. CO Adsorption on Clean and Oxidized Pd (111). *J. Phys. Chem. C* **2014**, *118* (111), 1118–1128. https://doi.org/10.1021/jp410895c.

(65) Nakamura, Y.; Kon, K.; Touchy, A. S.; Shimizu, K. I.; Ueda, W. Selective Synthesis of Primary Amines by Reductive Amination of Ketones with Ammonia over Supported Pt Catalysts. *ChemCatChem* **2015**, *7* (6), 921–924. https://doi.org/10.1002/cctc.201402996.

(66) Schreier, M.; Teren, S.; Belcher, L.; Regalbuto, J. R.; Miller, J. T. The Nature of "overexchanged" Copper and Platinum on Zeolites. *Nanotechnology* **2005**, *16* (7). https://doi.org/10.1088/0957-4484/16/7/036.

(67) Eskandari, S.; Dong, A.; De Castro, L. T.; AB Rahman, F. B.; Lipp, J.; Blom, D. A.; Regalbuto, J. R. Pushing the Limits of Electrostatic Adsorption: Charge Enhanced Dry Impregnation of SBA-15. *Catal. Today* **2019**, *338*. https://doi.org/10.1016/j.cattod.2019.06.082.

(68) Lucci, F. R.; Darby, M. T.; Mattera, M. F. G.; Ivimey, C. J.; Therrien, A. J.; Michaelides, A.; Stamatakis, M.; Sykes, E. C. H. Controlling Hydrogen Activation, Spillover, and Desorption with Pd-Au Single-Atom Alloys. *J. Phys. Chem. Lett.* **2016**, *7* (3), 480–485. https://doi.org/10.1021/acs.jpclett.5b02400.

(69) Zhang, X.; Ptasinska, S. High-Pressure-Induced Pseudo-Oxidation of Copper Surfaces by Carbon Monoxide. 2016, pp 1632–1635.

(70) Bukhtiyarov, A. V.; Prosvirin, I. P.; Saraev, A. A.; Klyushin, A. Y.; Knop-Gericke, A.; Bukhtiyarov, V. I. In Situ Formation of the Active Sites in Pd-Au Bimetallic Nanocatalysts for CO Oxidation: NAP (near Ambient Pressure) XPS and MS Study. *Faraday Discuss.* **2018**, *208*, 255–268. https://doi.org/10.1039/c7fd00219j.

(71) Mamatkulov, M.; Yudanov, I. V.; Bukhtiyarov, A. V.; Prosvirin, I. P.; Bukhtiyarov, V. I.; Neyman, K. M. Pd Segregation on the Surface of Bimetallic PdAu Nanoparticles Induced by Low Coverage of Adsorbed CO. *J. Phys. Chem. C* **2019**, *123* (13), 8037–8046. https://doi.org/10.1021/acs.jpcc.8b07402.

(72) Ichikawa, S.; Poppa, H.; Boudart, M. Disproportionation of CO on Small Particles of Silica-Supported Palladium. *J. Catal.* **1985**, *91*, 1–10.

(73) Li, C.; Sakata, Y.; Arai, T.; Domen, K.; Maruya, K.; Onishi, T. CO Disproportionation at Mild Temperatures over Partially Reduced Cerium Oxide. *J. Chem. Soc. Chem. Commun.* **1991**, No. 6, 410–411. https://doi.org/10.1039/C39910000410.

(74) Van Spronsen, M. A.; Daunmu, K.; O'Connor, C. R.; Egle, T.; Kersell, H.; Oliver-Meseguer, J.; Salmeron, M. B.; Madix, R. J.; Sautet, P.; Friend, C. M. Dynamics of Surface

869 Alloys: Rearrangement of Pd/Ag(111) Induced by CO and O2. *J. Phys. Chem. C* **2019**, *123*
870 (13), 8312–8323. https://doi.org/10.1021/acs.jpcc.8b08849.

871 (75) Hadjiivanov, K.; Venkov, T.; Knözinger, H. FTIR Spectroscopic Study of CO Adsorption
872 on Cu/SiO2: Formation of New Types of Copper Carbonyls. *Catal. Letters* **2001**, *75* (1–2),
873 55–59. https://doi.org/10.1023/A:1016759123842.

874 (76) Scarano, D.; Bordiga, S.; Lamberti, C.; Spoto, G.; Ricchiardi, G.; Zecchina, A.; Otero
875 Areán, C. FTIR Study of the Interaction of CO with Pure and Silica-Supported Copper (I)
876 Oxide. *Surf. Sci.* **1998**, *411* (3), 272–285. https://doi.org/10.1016/S0039-6028(98)00331-8.

877 (77) Meissner, H.; Gutschick, D.; Ewald, H.; Muller, H. The Influence of Support on the
878 Geminal Dicarbonyl Species RhI(CO)2 on Supported Rhodium Catalysts:An IR
879 Spectroscopic Study. *J. Mol. Catal.* **1986**, *36–37*, 359–373.

880 (78) Kaminski, P.; Ziolek, M.; Campo, B.; Daturi, M. FTIR Spectroscopic Study of CO
881 Oxidation on Bimetallic Catalysts. *Catal. Today* **2015**, *243* (x), 218–227.
882 https://doi.org/10.1016/j.cattod.2014.08.035.

883 (79) Venkov, T.; Hadjiivanov, K. FTIR Study of CO Interaction with Cu/TiO2. *Catal. Commun.*
884 **2003**, *4* (4), 209–213. https://doi.org/10.1016/S1566-7367(03)00035-9.

885 (80) Hadjiivanov, K. FTIR Study of Low-Temperature CO Adsorption on Cu / Silicalite-1. **2002**,
886 *3*, 37–44.

887 (81) Schumann, J.; Kröhnert, J.; Frei, E.; Schlögl, R.; Trunschke, A. IR-Spectroscopic Study on
888 the Interface of Cu-Based Methanol Synthesis Catalysts: Evidence for the Formation of a
889 ZnO Overlayer. *Top. Catal.* **2017**, *60* (19–20), 1735–1743. https://doi.org/10.1007/s11244-

017-0850-9.

(82) Hadjiivanov, K. I.; Kantcheva, M. M.; Klissurski, D. G. IR Study of CO Adsorption on Cu-ZSM-5 and CuO/SiO, Catalysts: **1996**, *92* (22), 4595–4600.

(83) Hadjiivanov, K.; Knözinger, H. FTIR Study of Low-Temperature CO Adsorption on Cu-ZSM-5: Evidence of the Formation of Cu2+(CO)2 Species. *J. Catal.* **2000**, *191* (2), 480–485. https://doi.org/10.1006/jcat.1999.2805.

(84) Rebelli, J.; Rodriguez, A. A.; Ma, S.; Williams, C. T.; Monnier, J. R. Preparation and Characterization of Silica-Supported, Group IB-Pd Bimetallic Catalysts Prepared by Electroless Deposition Methods. *Catal. Today* **2011**, *160* (1), 170–178. https://doi.org/10.1016/j.cattod.2010.06.011.

(85) Lear, T.; Marshall, R.; Lopez-Sanchez, J. A.; Jackson, S. D.; Klapötke, T. M.; Bäumer, M.; Rupprechter, G.; Freund, H. J.; Lennon, D. The Application of Infrared Spectroscopy to Probe the Surface Morphology of Alumina-Supported Palladium Catalysts. *J. Chem. Phys.* **2005**, *123* (17). https://doi.org/10.1063/1.2101487.

(86) Eischens, R. P.; Pliskin, W. A. The Infrared Spectra of Adsorbed Molecules. *Adv. Catal.* **1958**, *10*, 1–56. https://doi.org/10.1016/S0360-0564(08)60403-4.

(87) Yudanov, I. V; Sahnoun, R.; Neyman, K. M.; Ro, N.; Hoffmann, J.; Schauermann, S.; Joha, V.; Unterhalt, H.; Freund, H. CO Adsorption on Pd Nanoparticles : Density Functional and Vibrational Spectroscopy Studies. **2003**, 255–264. https://doi.org/10.1021/jp022052b.

(88) Cabilla, G. C.; Bonivardi, A. L.; Baltanás, M. A. Characterization by CO/FTIR Spectroscopy of Pd/Silica Catalysts and Its Correlation with Syn-Gas Conversion. *Catal.*

Letters **1998**, *55* (3–4), 147–156.

(89) Blyholder, G. Molecular Orbital View of Chemisorbed Carbon Monoxide. *J. Phys. Chem.* **1964**, *68* (10), 2772–2778. https://doi.org/10.1021/j100792a006.

(90) Bradshaw, A. M.; Hoffmann, F. M. The Chemisorption of Carbon Monoxide on Palladium Single Crystal Surfaces: IR Spectroscopic Evidence for Localised Site Adsorption. *Surf. Sci.* **1978**, *72* (3), 513–535. https://doi.org/10.1016/0039-6028(78)90367-9.

(91) Rebelli, J.; Detwiler, M.; Ma, S.; Williams, C. T.; Monnier, J. R. Synthesis and Characterization of Au–Pd/SiO2 Bimetallic Catalysts Prepared by Electroless Deposition. *J. Catal.* **2010**, *270* (2), 224–233. https://doi.org/10.1016/J.JCAT.2009.12.024.

(92) Giorgi, J. B.; Schroeder, T.; Bäumer, M.; Freund, H.-J. Study of CO Adsorption on Crystalline-Silica-Supported Palladium Particles. *Surf. Sci.* **2002**, *498* (1–2), L71–L77. https://doi.org/10.1016/S0039-6028(01)01756-3.

(93) Meunier, F. C. Relevance of IR Spectroscopy of Adsorbed CO for the Characterization of Heterogeneous Catalysts Containing Isolated Atoms. *J. Phys. Chem. C* **2021**, *125* (40), 21810–21823. https://doi.org/10.1021/acs.jpcc.1c06784.

(94) Bistoni, G.; Rampino, S.; Scafuri, N.; Ciancaleoni, G.; Zuccaccia, D.; Tarantelli, F. Chemical Science How p Back-Donation Quantitatively Controls the CO Stretching Response in Classical and Non- Classical Metal Carbonyl Complexes †. *Chem. Sci.* **2016**, *7*, 1174–1184. https://doi.org/10.1039/c5sc02971f.